Les Cahiers du GERAD ISSN: 0711–2440

Numerical evaluation of distributed wireless networks at scale

R. Khalvandi, B. Sansò

G–2026–03

January 2026

La publication de ces rapports de recherche est rendue possible grâce au soutien de HEC Montréal, Polytechnique Montréal, Université McGill, Université du Québec à Montréal, ainsi que du Fonds de recherche du Québec – Nature et technologies.

Dépôt légal – Bibliothèque et Archives nationales du Québec, 2026
– Bibliothèque et Archives Canada, 2026

The publication of these research reports is made possible thanks to the support of HEC Montréal, Polytechnique Montréal, McGill University, Université du Québec à Montréal, as well as the Fonds de recherche du Québec – Nature et technologies.

Legal deposit – Bibliothèque et Archives nationales du Québec, 2026
– Library and Archives Canada, 2026

GERAD HEC Montréal
3000, chemin de la Côte-Sainte-Catherine
Montréal (Québec) Canada H3T 2A7

Tél. : 514 340-6053
Téléc. : 514 340-5665
info@gerad.ca
www.gerad.ca

Numerical evaluation of distributed wireless networks at scale

Reza Khalvandi
Brunilde Sansò

Département de génie électrique, Polytechnique Montréal & GERAD, Montréal, (Qc), Canada, H3T 1J4

reza.khalvandi-ilezoole@polymtl.ca
brunilde.sanso@polymtl.ca

January 2026
Les Cahiers du GERAD
G–2026–03

Abstract : Large-scale distributed wireless networks offer infrastructure-free and cost-effective connectivity. Recent theoretical work has shown that scalability critically depends on underlying user interaction patterns; however, a fundamental gap remains between asymptotic feasibility results and concrete, numerically grounded performance metrics. This paper presents a comprehensive numerical evaluation of very large-scale distributed wireless networks by decomposing the cross-layer P2P capacity analysis into two tightly coupled components: the expected hop count $\mathbf{E}(h)$ and the effective single-hop transmission capacity $\mathbf{E}(C_{\text{eff}})$. Leveraging network symmetry and geometric partitioning, we transform the discrete hop-count problem into a continuous formulation and derive a closed-form integral upper bound on $\mathbf{E}(h)$ using convex optimization. This enables efficient numerical evaluation even for networks with millions of nodes and reveals that, despite network diameters spanning hundreds of kilometers, typical communication paths traverse only a small fraction of this extent under real-world interaction patterns. To quantify $\mathbf{E}(C_{\text{eff}})$, we develop a cross-layer wireless model with full spatial reuse and derive a closed-form upper bound on aggregate interference, allowing optimization of the resource-sharing parameter that maximizes per-node throughput. Combining both components yields explicit numerical bounds on link-level capacity, end-to-end P2P throughput, delay, spectral efficiency, and energy consumption. The results demonstrate that large-scale distributed networks can sustain substantial per-user data volumes while operating with limited spectrum and ultra-low transmit power. Short-range links enable aggressive spatial reuse and high energy efficiency, and naturally align with millimeter-wave technologies that provide large bandwidths. Overall, this work shows that large-scale distributed wireless networks are not only theoretically scalable but also practically competitive with infrastructure-based systems.

Keywords : Large-scale distributed wireless networks; multi-hop routing; point-to-point capacity; spatial reuse; energy-efficient networking

1 Introduction

Distributed wireless networks—capable of supporting vast numbers of devices over wide geographic areas without relying on fixed infrastructure—represent one of the most transformative directions in next-generation communication. Distributed wireless networks operate through multi-hop communication, in which devices cooperatively relay data for one another across multiple wireless links, enabling end-to-end connectivity. Numerous emerging applications increasingly depend on such architectures. Distributed networking underpins a wide range of modern systems, including real-time vehicular coordination [38], cooperative UAV sensing and control [10, 36], and large-scale agricultural monitoring and automation [20, 51]. It is also a core enabler of smart-city infrastructures and massive IoT deployments [6, 7], while forming the foundation of edge and collaborative computing paradigms [26, 43] and decentralized, federated, and swarm-based artificial intelligence [11, 37]. Many of these applications involve extremely large numbers of devices and demand real-time or near-real-time communication—making scalable distributed wireless networking increasingly indispensable. Recent technological progress strengthens the case for large-scale distributed networks. Advances in artificial intelligence, precise positioning, blockchain, and distributed processing [54] enhance network autonomy. Higher device density improves connectivity even as it complicates routing. Modern devices provide more accurate sensing, larger memory, and longer battery life, enabling reliable neighborhood estimation, efficient route computation [8, 44], and increased buffering capacity. Reinforcement learning methods implemented in a distributed fashion [12, 13, 22, 52, 56] have shown strong potential for managing dynamic topologies and highly variable interference environments, paving the way toward scalable distributed wireless networks [44].

For more than two decades, theoretical works have doubted on whether such networks can scale at all. Gupta and Kumar [19] famously disagreed on scalability, whereas later studies [2, 31] argued that scalability may be achievable under specific distance-dependent interaction models. However, these conditions were never validated using real-world interaction data. In our earlier work [24], we addressed this gap by focusing on the core abstraction governing scalability: the expected number of hops and its impact on point-to-point (P2P) capacity. Using real-world human interaction models and power-law kernels extracted from statistical datasets, we demonstrated—for the first time—that distributed wireless networks may indeed scale without catastrophic capacity collapse. This result established a solid theoretical foundation, but left open the numerical and practical questions that arise when moving toward real engineering constraints. The challenge is that asymptotic results alone are insufficient. Quantifying delay, spectrum requirements, achievable throughput, and energy feasibility for real devices (e.g., smartphones or low-power IoT nodes) requires explicit modeling of physical-layer effects, exact hop counts, interference, and the energy cost of multi-hop forwarding—factors that cannot be abstracted away. Moreover, engineering-oriented evaluation demands concrete numerical values rather than scaling laws: What data rates are achievable per node? How does delay behave in practical regimes? Can current hardware sustain continuous connectivity? And how much bandwidth is required to meet real-time and non-real-time QoS constraints?

To answer such questions in manageable way, some analytical structure must be preserved. Following our earlier approach [24], we adopt a symmetric hexagonal network topology, which captures the geometric essence of dense networks while avoiding unnecessary routing complexities. Although idealized, this topology naturally appears in real scenarios such as UAV formations, satellite constellations, smart agriculture, and planned mesh deployments [9, 33]. Most importantly, its symmetry enables exact numerical evaluation of hop count and cross-layer interference, providing a fundamental baseline for what is theoretically achievable under optimal structural conditions in a massive scale distributed networking . Building on this structured model, we deliver the first numerical, cross-layer assessment of practical P2P capacity for large-scale distributed wireless networks. Specifically, we introduce a rigorous capacity framework that decomposes the problem into two tightly coupled components: the expected hop count $\mathbf{E}(h)$ in a P2P connection and the effective per-node transmission capacity $\mathbf{E}(C_{\text{eff}})$. The term $\mathbf{E}(C_{\text{eff}})$ represents the average amount of traffic that a node can successfully transmit over

an active link in one hop, after accounting for spatial reuse and the area dedicated to each active transmission. Our main contributions are summarized as follows:

- Leveraging network symmetry, we derive a closed-form integral expression that upper-bounds $\mathbf{E}(h)$, enabling efficient numerical evaluation even for extremely large networks. To compute $\mathbf{E}(h)$, we adopt a power-law interaction model with parameters extracted from real-world data. By transforming the discrete hop-count problem into a continuous geometric formulation and applying convex-analytic techniques, we obtain an expression that is validated by discrete hop-count simulations across a wide range of interaction parameters. The numerical results further reveal that, under empirically observed interaction patterns, even when the physical network spans hundreds of kilometers, typical end-to-end communications traverse only a small fraction of this extent. Beyond numerical accuracy, the closed-form expression offers structural insight into how the interaction pattern behaves across different regions of the network—highlighting, in particular, boundary effects and the concentration of interactions near the network center.
- We construct a cross-layer wireless model that permits full resource sharing among active links and derive a closed-form upper bound on cross-interference. This formulation allows us to optimize the resource-sharing factor that maximizes the effective per-node single-hop transmission capacity $\mathbf{E}(C_{\text{eff}})$. Unlike previous heuristic choices, the optimized sharing value yields substantial improvements in network throughput. This analysis also characterizes the spatial structure of interference in dense distributed networks. By quantifying how interference accumulates across concentric transmitter rings, we show that the dominant contribution arises from nearby transmitters, while aggregate interference from distant nodes is negligible.
- Combining the results for $\mathbf{E}(h)$ and $\mathbf{E}(C_{\text{eff}})$, we obtain the first numerical evaluation of point-to-point capacity in large-scale distributed wireless networks, enabling explicit upper bounds on the expected hop count, link-level capacity, and end-to-end P2P throughput. Beyond the specific network model and assumptions, the analysis provides detailed insight into achievable delay, data rate, spectral efficiency, and energy consumption, and shows that even at extreme scales and with low-power devices, distributed networks can remain efficient and resilient. The performance gains arise from two fundamental properties shared by nearly all network topologies and physical-layer technologies. First, realistic interaction patterns reveal that expected hop counts are orders of magnitude smaller than classical pessimistic estimates, removing the presumed scalability bottleneck of multi-hop communication. Second, short communication links inherently optimize network performance by enabling aggressive spatial reuse and ultra-low power operation. This short-link regime naturally aligns with millimeter-wave technologies, unlocking large bandwidths while sustaining high throughput and energy efficiency in large-scale distributed networks.

The rest of the paper is organized as follows. Section 2 presents the related work and provides the necessary preliminary background. Section 3 describes the network model and the overall problem formulation. Section 4 details the computation of the numerical expected hop count. Section 5 explains the calculation of the effective per-node single-hop transmission capacity and the corresponding optimization procedure. Section 6 presents the numerical performance evaluation results, and Section 7 concludes the paper.

2 Background and problem overview

The central question in large-scale distributed wireless networking is whether a fully infrastructure-free system can sustain meaningful communication rates as the number of nodes grows. Classical capacity-scaling results for ad hoc networks—starting from the seminal work of Gupta and Kumar [19] and followed by numerous extensions [1, 14, 16, 17, 29, 41, 42, 50, 55]—have shown that multi-hop routing, interference, and spatial reuse jointly determine the point-to-point (P2P) capacity of large networks.

In our previous work [24], we formalized this dependence through the inequality

$$C_{P2P} \leq \frac{\mathbf{E}(C_L)}{\mathbf{E}(h)\,\mathbf{E}(A_\rho)}, \tag{1}$$

where C_{P2P} denotes the expected P2P capacity (average rate available to communicate with an arbitrary destination), $\mathbf{E}(C_L)$ is the expected capacity of an active wireless link, $\mathbf{E}(h)$ is the expected hop count between random source–destination pairs, and $\mathbf{E}(A_\rho)$ is the expected normalized area per active link, which captures spatial reuse and hence the effective number of simultaneously active links. The density parameter $\rho = n/A_{\text{net}}$ relates $\mathbf{E}(A_\rho)$ to the node placement and transmission range. Existing capacity studies have repeatedly shown that, across a wide variety of physical-layer and MAC-layer models, $\mathbf{E}(C_{\text{eff}})$ typically scales as $\Theta(W)$, where W is the available bandwidth [16, 19, 48, 50], while the expected hop count $\mathbf{E}(h)$ and the underlying interaction model over distance can fundamentally change the asymptotic behavior of C_{P2P}: depending on the power-law exponent α, capacity can range from strongly decreasing with n to remaining essentially constant [2, 18, 23, 31, 50, 55]. In [24], we exploited realistic, data-driven power-law interaction models to extract α from empirical studies of social interactions [3–5, 25, 27, 28, 30, 32, 40, 45], and showed that large-scale distributed networks are asymptotically feasible: even for tens of millions of nodes, the expected hop count remains bounded by a constant or grows only very slowly, implying that the order of C_{P2P} can remain practically acceptable.

In the present work, our goal is no longer limited to asymptotic feasibility. We seek *numerical* estimates of P2P capacity and Quality-of-Service (QoS) metrics (data rate, delay, energy efficiency) for realistic network sizes. To keep the notation focused on the two dominant factors—path length and per-node transmission capability—we group the geometric reuse term $\mathbf{E}(A_\rho)$ with the link capacity and define an effective per-node transmission term

$$\mathbf{E}(C_{\text{eff}}) \triangleq \frac{\mathbf{E}(C_L)}{\mathbf{E}(A_\rho)}. \tag{2}$$

With this definition, the bound (1) can be rewritten as

$$C_{P2P} \leq \frac{\mathbf{E}(C_{\text{eff}})}{\mathbf{E}(h)}. \tag{3}$$

The key challenge is therefore twofold: (i) to accurately compute the expected hop count $\mathbf{E}(h)$, and (ii) to model and optimize a realistic effective per-node single-hop transmission capacity $\mathbf{E}(C_{\text{eff}})$ for a dense, multi-hop wireless system. Only limited prior work has jointly examined physical-layer and MAC-layer effects in a unified capacity estimation framework. In [35], the authors investigate the link-layer throughput capacity of MIMO ad hoc networks by evaluating how each link utilizes spatial resources based on its actual interference impact on other links. Their analysis derives the number of simultaneously active links and the achievable data rates within a given region. Similarly, [47] derives upper and lower bounds on the transmission capacity of ad hoc networks where nodes employ multiple antennas. Other studies have examined transmission capacity under different PHY/MAC assumptions. For instance, [49] analyzes CDMA-based ad hoc networks in which nodes are distributed according to a Poisson point process, deriving upper and lower bounds for both FH-CDMA and DS-CDMA systems. In another related work, [34] develops a stochastic-geometry framework to evaluate the performance of SCMA ad hoc networks. The improvements introduced in this work for computing $\mathbf{E}(C_{\text{eff}})$—relative to a simple unidirectional model—provide a foundation for evaluating the numerical performance of large-scale distributed networks when equipped with modern transmission technologies that can significantly enhance distributed networking capacity.

Directly estimating C_{P2P} is a cross-layer problem: routing decisions, spatial reuse, interference, and physical-layer constraints all interact in a highly non-linear way. To keep the analysis tractable while preserving the essential physics, we decompose the problem into two tightly coupled subproblems:

- *Subproblem 1: Expected hop count for P2P connections.* Given a network of n nodes and an interaction model $P(d)$, we compute $\mathbf{E}(h)$ between a random source–destination pair under optimal routing.
- *Subproblem 2: Expected transmission rate per node.* For a given spatial reuse pattern and interference model, we determine the expected per-node transmission rate $\mathbf{E}(C_{\text{eff}})$, accounting for cross-layer constraints such as SINR thresholds, scheduling, and resource sharing.

Although these subproblems are interdependent, treating them separately enables a modular analysis: *Subproblem 1* captures the large-scale geometric and probabilistic structure of multi-hop communication, while *Subproblem 2* encapsulates PHY/MAC-layer constraints and resource allocation. Furthermore, our goal here is to obtain a *numerical* characterization of performance. This is intrinsically a multi-layer problem: for general network settings a closed-form solution is unlikely, and faithful large-scale simulations (millions of nodes, billions of potential connections) are computationally prohibitive. Moreover, optimal routing algorithms and metrics for such scales are not yet available; consequently, performance achieved by currently available algorithms can be orders of magnitude sub-optimal at million-node scales and may not reflect the true potential of large-scale distributed networking. To address these challenges, we adopt a *symmetric* node arrangement. First, this symmetry markedly reduces modeling complexity and enables closed-form expressions for per-node capacity across network sizes. Second, under this arrangement the physical shortest path coincides with the optimal route (under our interference and path-loss assumptions), allowing us to evaluate the *actual* potential of the architecture without confounding algorithmic sub-optimality. This provides a pragmatic shortcut to quantify QoS KPIs and energy consumption with limited computational resources.

Finally, We estimate the average P2P capacity C_{P2P} by combining the expected number of hops $\mathbf{E}(h)$ and the expected link capacity $\mathbf{E}(C_{\text{eff}})$. We evaluate network performance based on Quality of Service (QoS) parameters, using the estimated C_{P2P}. This evaluation provides insights into how such a massive-scale could preform for different data usage and its energy efficiency and flexibility.

3 Network model and problem structure

We consider a large-scale distributed wireless network composed of n nodes arranged on a hexagonal lattice. This symmetric topology—depicted in Figure 1—serves two purposes. First, it preserves the geometric essence of dense networks while avoiding the irregularities and routing ambiguities that arise in random deployments. Second, it enables closed-form analysis of both hop-count scaling and interference, thereby providing a clean upper bound on performance under ideal spatial organization. Each node occupies a hexagonal region of area $d_0^2\sqrt{3}/2$, where d_0 is the nearest–neighbor spacing. Consequently, the total network area is $A_{\text{net}} = n\frac{\sqrt{3}}{2}d_0^2$, and the equivalent square side length is

$$L = \sqrt{A_{\text{net}}} = \sqrt{\tfrac{\sqrt{3}}{2}}\, d_0\sqrt{n}. \tag{4}$$

3.1 Subproblem 1: Expected hop count $\mathbf{E}(h)$ upper bound

In this arrangement, communication between nodes follows a distance-dependent interaction probability $P(d)$. Motivated by empirical studies of social and human mobility networks [3, 5, 28], we adopt a modified power-law form

$$P(d) = \frac{P_0}{(d+\beta_0)^{\alpha}}. \tag{5}$$

Here, α is the power-law exponent governing the decay of long-range interactions, and β_0 is a small offset derived from real-world datasets to account for short-distance saturation effects. The normalization parameter P_0 ensures that the interaction probabilities of each node sum to one.

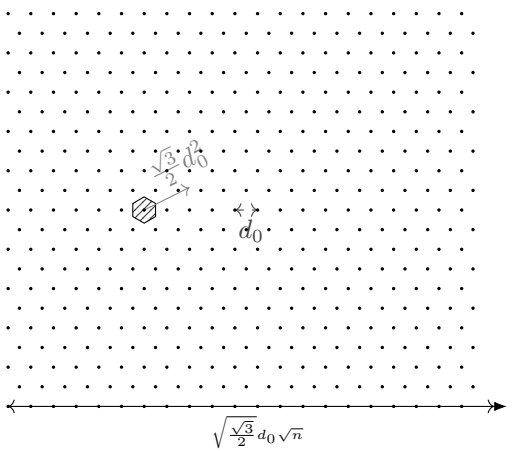

Figure 1: Regular hexagonal lattice used to model a large-scale distributed network. Nodes are uniformly spaced by distance d_0, inducing a network diameter that scales as $\sqrt{\frac{\sqrt{3}}{2}}\,d_0\sqrt{n}$. The shaded hexagon represents the area per node.

To make the expected hop count computation tractable, we leverage the symmetry of the lattice and decompose the process into two phases. In the first phase, we compute the hop count for a source at the network center, where rotational symmetry simplifies normalization and interaction calculations. In the second phase, we extend this result to the entire network by analyzing how normalization constants vary with the source location and showing that the central value serves as a tight global upper bound. The technical details of each phase are summarized below.

3.1.1 Phase 1: Expected hop count for the central node

The source node is positioned at the geometric center of the network. Under this placement, symmetry ensures uniform angular distribution of nodes at equal distance.

1. **Probability normalization parameter P_0^c:** Compute the value of P_0 that ensures

$$\sum_{j \neq i} P(d_j) = 1,$$

   where i is the central node. This yields an upper-bound normalization constant P_0^c, because the center has the largest number of nodes at each distance d.
2. **Central hop-count expression:** Using P_0^c, compute the expected hop count for the central node, $\mathbf{E}(h)^c$.

Nodes are first aggregated into concentric rings centered at the source node. For each ring, the distance-dependent interaction probability is evaluated, and its contribution to the expected hop count is computed based on the corresponding hop distance. The resulting discrete summation over rings is then approximated by a continuous integral in the radial domain. Solving this integral yields a closed-form expression for the expected hop count $\mathbf{E}(h)^c$. Finally, the derived expression is validated against discrete hop-count simulations over a wide range of (α, β_0) parameters, demonstrating close agreement and confirming that the model accurately captures structural effects such as boundary sensitivity and the central concentration of interactions.

3.1.2 Phase 2: Extending result to the entire network

1. **Location-dependent normalization:** Using convex-analytic and geometric arguments, we characterize how the normalization constant P_0 varies with the source location. Its maximum occurs at network corners, while it decreases rapidly when moving toward the center.

2. **Dominance of the central hop count:** For almost all interior nodes, the normalization constant is close to P_0^c, implying that their expected hop count cannot exceed $\mathbf{E}(h)^c$ by more than a small margin.
3. **Global approximation:** We show that $\mathbf{E}(h)^c$ forms a tight upper bound for the network-wide average hop requirement.

Because normalization constants and hop distances converge quickly to their central-node values for almost all source locations, the average expected hop count for the entire network is well approximated by the analytically derived central hop count $\mathbf{E}(h)^c$.

3.2 Subproblem 2: Effective per-node transmission capacity

The second component of the capacity problem concerns the rate at which each node can transmit information over an active link. We model a fully reusable wireless medium in which concurrent transmissions share the entire available spectrum, subject to spatial separation constraints. To guarantee signal quality—analogous to the protocol model—we reserve a protection area around each active transmission. This reserved area scales as $(1+\Delta)^2$, where Δ denotes the reuse spacing parameter. Accordingly, the expected normalized area consumed per active link is

$$\mathbf{E}(A_\rho) = (1+\Delta)^2.$$

Under this reuse model, let $\mathbf{E}(C_L)$ denote the expected link capacity. Normalizing by the spatial reuse factor yields the effective per-node capacity (using Equation (2))

$$\mathbf{E}(C_{\text{eff}}) = \frac{\mathbf{E}(C_L)}{(1+\Delta)^2}. \tag{6}$$

A larger value of Δ improves SINR and therefore increases $\mathbf{E}(C_L)$, but simultaneously decreases reuse by enlarging the exclusion area. We derive the upper bound on aggregate interference experienced by a central receiver, approximate its average value across the network, compute $\mathbf{E}(C_L)$ as a function of Δ and the path-loss exponent, and identify the optimal Δ that maximizes $\mathbf{E}(C_{\text{eff}})$. Additional details of the communication model are provided in Section 5.

3.3 Problem integration

The upper bound of overall point-to-point capacity for a random source–destination pair satisfies

$$C_{P2P} \leq \frac{\mathbf{E}(C_{\text{eff}})}{\mathbf{E}(h)}.$$

Thus, the network's performance depends jointly on (i) how far information must travel (captured by $\mathbf{E}(h)$), and (ii) how efficiently nodes can transmit information in each hop (captured by $\mathbf{E}(C_{\text{eff}})$). In the remainder of the paper, we derive these two quantities in detail and use them to estimate numerical P2P capacity and QoS metrics.

4 Subproblem 1: Expected number of hops estimation

The quantity $\mathbf{E}(h)$ represents the average expected number of hops between a node and all other nodes in a P2P connection across the entire network. To estimate this, we first calculate the upper bound of the hop count for the central node, denoted $\mathbf{E}(h)^c$, and then prove that $\mathbf{E}(h)^c$ also bounds the average $\mathbf{E}(h)$ over the entire network.

As discussed in Section 3, the interaction probability between a source and destination depends solely on their distance d and follows a power-law distribution with an offset parameter β_0. For the central node, this distribution is written as

$$P(d) = \frac{P_0^c}{(d+\beta_0)^\alpha}\,. \tag{7}$$

where P_0^c ensures the total interaction probability sums to 1 for the central node and P_0 may differ for nodes in other network locations.

4.1 $\mathbf{E}(h)$ for the node at the center of the network

4.1.1 Compute the P_0 constant

We consider a source node located at the center of the network, as depicted in Figure 2, which selects a destination node j from the $n-1$ nodes with probability p_j. The sum of all interaction probabilities with the source node must satisfy:

$$\sum_{j=1}^{n-1} p_j = 1\,. \tag{8}$$

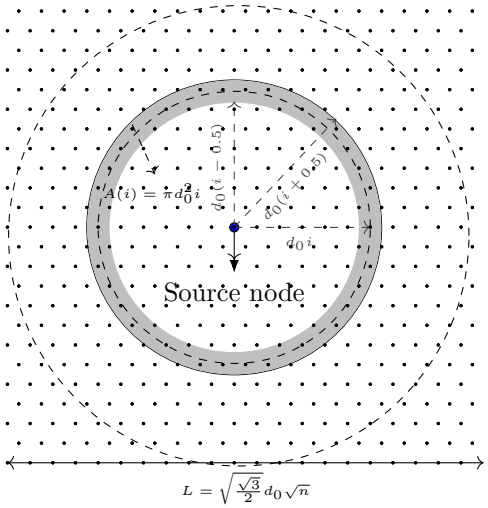

Figure 2: Geometric partitioning of the hexagonal lattice into concentric rings centered at the source node. All nodes within ring i lie at approximately the same distance id_0 from the source, allowing the interaction probability to be evaluated ring-by-ring.

According to the interaction probability model in Equation (7), all nodes at the same distance from a given source node have the same interaction probability. Building on this idea and the reformulation in Equation (8), we partition the network area into concentric rings around the source node, as shown in Figure 2. Each ring i is centered at the source node with radius id_0, covering the area between two circles of radii $d_0(i-0.5)$ and $d_0(i+0.5)$. We approximate that all nodes within ring i have the same interaction probability $P(id_0)$. Thus, the total interaction probability for ring i is

$$P(id_0) \cdot N(id_0),$$

where $N(id_0)$ is the number of nodes in ring i. By Covering the entire network with these rings Equation (8) is written as:

$$\sum_{i=1}^{i_{\max}} P(id_0) \cdot N(id_0) = \sum_{j=1}^{n-1} p_j = 1. \tag{9}$$

As shown in Figure 1, each node effectively occupies an area of $d_0^2\sqrt{3}/2$, implying a node density of $\rho = 2/(\sqrt{3}d_0^2)$. To find the number of nodes in ring i, we calculate the area $A(i)$ between circles of radii $d_0(i-0.5)$ and $d_0(i+0.5)$ (see Figure 2). Thus, the number of nodes in ring i is

$$N(id_0) = \rho\, A(i) = \rho\,\pi\Big[(d_0(i+0.5))^2 - (d_0(i-0.5))^2\Big] = \frac{4\pi}{\sqrt{3}}\, i, \tag{10}$$

To account for the network node interaction probability with the source node, which should equals to 1 , we substitute $N(id_0)$ from Equation (10) and $P(id_0)$ from Equation (7) into Equation (9), giving:

$$\sum_{i=1}^{i_{\max}} \frac{4\pi i}{\sqrt{3}} \cdot \frac{P_0^c}{(id_0+\beta_0)^\alpha} = \frac{P_0^c 4\pi}{d_0^\alpha\sqrt{3}} \sum_{i=1}^{i_{\max}} \frac{i}{(i+\frac{\beta_0}{d_0})^\alpha} = 1. \tag{11}$$

Since the network is square, the area cannot be covered exclusively by complete circular rings; hence a single global $i_{\max}$ does not satisfy Equation (11). Thus, we partition the rings into small angular arcs of width $\delta\vartheta$ for $0 \le \vartheta \le 2\pi$, let $i_{\max}(\vartheta)$ denote the maximum number of rings along direction ϑ, and then sum over all arcs. In the limit $\delta\vartheta \to 0$, this yields the integral

$$\frac{2P_0^c}{\sqrt{3}\,d_0^\alpha} \int_0^{2\pi} \sum_{i=1}^{i_{\max}(\vartheta)} \frac{i}{\left(i+\frac{\beta_0}{d_0}\right)^\alpha}\, \mathrm{d}\vartheta = 1. \tag{12}$$

Now set $\beta = \beta_0 d_0$ and define $f(r,\vartheta) = r/(r+\beta)^\alpha$, which is symmetric in ϑ and monotonically decreasing in r for $r \gg \beta$. Based on Theorem 11, we lower-bound the area integral over the square by integrating over 12 polar sectors (anchored at the origin): eight sectors with radial extent $L/2$ and four sectors with radial extent $L/\sqrt{3}$, each with angular width $\pi/6$. Substituting the network side length L from Equation (4), the corresponding ring counts are

$$i_{\max}^{(8)} = \frac{L}{2d_0} = \sqrt{\frac{\sqrt{3}\,n}{8}}, \qquad i_{\max}^{(4)} = \frac{L}{\sqrt{3}\,d_0} = \sqrt{\frac{n}{2\sqrt{3}}}.$$

Therefore, the integral over network is lower bounded by

$$\begin{aligned}\int_{\text{Square}} f(r,\vartheta)\,\mathrm{d}r\,\mathrm{d}\vartheta \ge (8\tfrac{\pi}{6} &\int_0^{\sqrt{\frac{\sqrt{3}\,n}{8}}} \frac{r}{(r+\beta)^\alpha}\,\mathrm{d}r \\ &+ 4\tfrac{\pi}{6} \int_0^{\sqrt{\frac{n}{2\sqrt{3}}}} \frac{r}{(r+\beta)^\alpha}\,\mathrm{d}r).\end{aligned} \tag{13}$$

Moreover, from Theorem 8, which provides a lower bound by replacing the discrete series with an integral, reintegrating over ϑ from both sides yields

$$\int_0^{2\pi} \sum_{i=1}^{i(\vartheta)} \frac{i}{(i+\beta)^\alpha}\, d\vartheta \ge \int_0^{2\pi} \int_0^{i(\vartheta)} \left(\frac{r}{(r+\beta)^\alpha} - \frac{(\alpha-1)^{\alpha-1}}{\alpha^\alpha \beta^{\alpha-1}}\right) dr\, d\vartheta. \tag{14}$$

The left-hand side of Equation (14) equals $\frac{\sqrt{3}}{2}P_0^c$ times the total interaction probability with all nodes (normalized to 1), see Equation (11). Therefore, using the lower bound of the integral over the square form Equation (13), we obtain

$$\frac{4\pi P_0^c}{3\sqrt{3}d_0^\alpha}\Big(\begin{array}{c} 2\int_0^{\sqrt{\frac{\sqrt{3}\,n}{8}}} \frac{r}{(r+\beta)^\alpha}\,\mathrm{d}r + \int_0^{\sqrt{\frac{n}{2\sqrt{3}}}} \frac{r}{(r+\beta)^\alpha}\,\mathrm{d}r \\ -\frac{3(\alpha-1)^{\alpha-1}}{\alpha^\alpha\beta^{\alpha-1}} \end{array} \Big) \le 1.$$

Now, the indefinite integral W is

$$W(r,\alpha,\beta) = \int \frac{r}{(r+\beta)^{\alpha}}\,dr = -\frac{(r+\beta)^{1-\alpha}((\alpha-1)r+\beta)}{(\alpha-1)(\alpha-2)}. \tag{15}$$

For compactness, define

$$U(\alpha,\beta) = W(0,\alpha,\beta) - \frac{(\alpha-1)^{\alpha-1}}{\alpha^{\alpha}\beta^{\alpha-1}}. \tag{16}$$

Thus, the refined upper bound for P_0^c can be written as

$$P_0^c \leq \frac{\sqrt{3}d_0^{\alpha}}{4\pi(U(\alpha,\beta) - \frac{1}{3}(2W(\sqrt{\frac{\sqrt{3}n}{8}},\alpha,\beta) + W(\sqrt{\frac{n}{2\sqrt{3}}},\alpha,\beta)))}. \tag{17}$$

Finally, as the network size grows without bound ($n \to \infty$), the asymptotic upper bound simplifies to

$$\lim_{\sqrt{n}\to\infty} P_0^c \leq \frac{\sqrt{3}d_0^{\alpha}(\alpha-1)(\alpha-2)}{4\pi(\frac{1}{\beta^{\alpha-2}} - \frac{(\alpha-2)(\alpha-1)^{\alpha}}{\alpha^{\alpha}\beta^{\alpha-1}})}. \tag{18}$$

4.1.2 Compute $\mathbf{E}(h)$ using P_0

To calculate $\mathbf{E}(h)^c$, we adopt a methodology analogous to the computation of P_0^c in the previous subsection. Instead of circular rings based on equal physical distances, we consider nested hexagonal rings that each represent equal graph metric distances (hop counts) from the source node. In fact, nodes equidistant in terms of hop count from the source node form hexagons centered on the source node. For example, in Figure 3, we can see that all nodes with a two-hop distance from the central node ($h_{2j} = 2$) form a hexagon. Constructing these hexagons for all possible hop counts results in a series of nested hexagonal rings around the source node. The expected value $\mathbf{E}(h)$ can be expressed using the law of total expectation:

$$\mathbf{E}(h)^c = \sum_{i=1}^{i_{\max}} \mathbf{E}(h \mid h = i)P(h = i),$$

where $i \in \{1, 2, \ldots, i_{\max}\}$ represents the ring number corresponding to the hop count. Since all nodes within the same ring have the same hop count ($h_{ij} = i$), the conditional expectation simplifies to $\mathbf{E}(h \mid h = i) = i$. Substituting this into the equation, we obtain:

$$\mathbf{E}(h)^c = \sum_{i=1}^{i_{\max}} i \cdot P(h = i).$$

Here, $P(h = i)$ is the probability that a node belongs to the i^{th} ring, which can be calculated as:

$$P(h = i) = \sum_{j=1}^{j(i)} P(d_{ij}),$$

where $j(i)$ denotes the number of nodes in the i^{th} ring, and $P(d_{ij})$ is the probability associated with each node j in that ring. Consequently, the expected number of hops per ring, $\mathbf{E}(h_i)$, is defined as:

$$\mathbf{E}(h_i) = i \cdot \sum_{j=1}^{j(i)} P(d_{ij}).$$

Summing over all possible rings, the total expected number of hops is given by:

$$\mathbf{E}(h) = \sum_{i=1}^{i_{\max}} \mathbf{E}(h_i). \tag{19}$$

In each ring, the hop count distance of node j from the source node (h_{ij}) equals the ring number ($h_{ij} = i$). Substituting the interaction probability from Equation (7) yields:

$$\mathbf{E}(h_i) = \sum_{j=1}^{j(i)} i \frac{P_0^c}{(d_{ij} + \beta_0)^\alpha}. \tag{20}$$

For the first hexagon ($i = 1$), there are six nodes ($j(1) = 6$), all located at a distance $d_{1j} = d_0$ from the source node. The expected number of hops for the first ring is thus:

$$\mathbf{E}(h_1) = \sum_{j=1}^{6} \frac{P_0^c}{(d_0 + \beta_0)^\alpha} = \frac{6P_0^c}{(d_0 + \beta_0)^\alpha}. \tag{21}$$

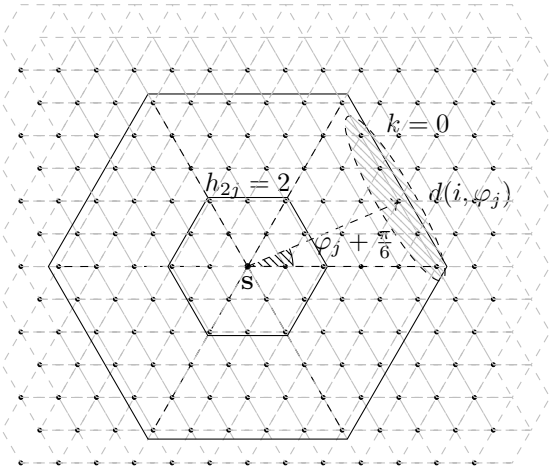

Figure 3: Sectorization of the i^{th} hexagonal ring used in the computation of $\mathbf{E}(h)$. Each ring with $i \geq 2$ is divided into six identical sectors, each spanning $\pi/3$ radians and containing i nodes. The figure illustrates the sector indexed by $k = 0$, where the position of node ij is parameterized by the angular offset φ_j from the sector's central axis. The distance from the source to node ij is thus given by $d(i, \varphi_j)$ in Equation (22), with $-\pi/6 < \varphi_j \leq \pi/6$.

For each hexagonal ring with ring number $i \geq 2$ surrounding the source node, we divide the ring into six identical sectors. Each sector spans an angle of $\frac{\pi}{3}$ radians and contains i nodes. In Figure 3, we illustrate the nodes within the sector labeled $k = 0$ of the i^{th} ring. The distance from the source node to a node ij within this sector is denoted by $d(i, \varphi_j)$. The angle φ_j is defined as the angle between the sector's central axis (the line bisecting the sector) and the line segment connecting the source node to node ij. In other words, φ_j measures the deviation of node ij from the sector's central direction. This angle satisfies:

$$-\frac{\pi}{6} < \varphi_j \leq \frac{\pi}{6}.$$

As derived in Theorem 1, the distance between any node in the sector and the source node is given by:

$$d(i, \varphi_j) = \frac{d_0 i \cos(\frac{\pi}{6})}{\cos(\varphi_j)}. \tag{22}$$

Now, each ring contains six sectors, and each sector consists of i nodes. The expected hop distance, $\mathbf{E}(h_i)$, by substituting $d(i,\varphi_j)$ into Equation (20) and defining $\beta = \beta_0/d_0$, can be expressed as:

$$\mathbf{E}(h_i) = 6(\sum_{j=1}^{i} \frac{P_0^c i}{(d(i,\varphi_j)+\beta_0)^\alpha}) = 6\sum_{j=1}^{i} \frac{P_0^c i}{d_0^\alpha (\frac{i\cos(\frac{\pi}{6})}{\cos(\varphi_j)}+\beta)^\alpha}. \tag{23}$$

Now, by multiply and dividing to $\pi/3i$, we can create a Riemann sum approximation as:

$$\mathbf{E}(h_i) = \frac{18P_0^c}{\pi d_0^\alpha}(\frac{\pi}{3i}\sum_{j=1}^{i} \frac{i^2}{(\frac{i\cos(\frac{\pi}{6})}{\cos(\varphi_j)}+\beta)^\alpha}).$$

The term inside the parentheses approximated by:

$$\int_{-\frac{\pi}{6}}^{\frac{\pi}{6}} \frac{i^2}{(\frac{i\cos(\frac{\pi}{6})}{\cos(\varphi)}+\beta)^\alpha}\, d\varphi = 2\int_{0}^{\frac{\pi}{6}} \frac{i^2}{(\frac{i\cos(\frac{\pi}{6})}{\cos(\varphi)}+\beta)^\alpha}\, d\varphi.$$

Thus,$\mathbf{E}(h_i)$ the discrete summation can be approximated as follows:

$$\mathbf{E}(h_i) \approx \frac{36P_0^c}{\pi d_0^\alpha}\int_{0}^{\frac{\pi}{6}} \frac{i^2}{(\frac{i\cos(\frac{\pi}{6})}{\cos(\varphi)}+\beta)^\alpha}\, d\varphi. \tag{24}$$

Thus, by substitute this integral in Equation (23) the expected hop count for all rings beyond the first ($i = 2$ to $i_{\max}$) can be approximated as:

$$\sum_{i=2}^{i_{\max}} \mathbf{E}(h_i) = \frac{36P_0}{\pi d_0^\alpha}\sum_{i=2}^{i_{\max}}\int_{0}^{\frac{\pi}{6}} \frac{i^2}{(\frac{i\cos(\frac{\pi}{6})}{\cos(\varphi)}+\beta)^\alpha}\, d\varphi\,. \tag{25}$$

Further, as shown in Theorem 9, the upper bound $\sum_{i=2}^{i_{\max}}\int_0^{\frac{\pi}{6}} i^2/(\frac{i\cos(\frac{\pi}{6})}{\cos(\varphi)}+\beta)^\alpha\, d\varphi$ of this summation can be expressed as:

$$\int_{2}^{i_{\max}}\int_{0}^{\frac{\pi}{6}} \frac{r^2}{(\frac{r\cos(\frac{\pi}{6})}{\cos(\varphi)}+\beta)^\alpha}\, d\varphi\, dr + \frac{(\alpha-2)^\alpha(2\sqrt{3}+\frac{4\pi}{3})}{3\beta^{\alpha-2}\alpha^\alpha}. \tag{26}$$

Finally, by substituting the value of $\mathbf{E}(h_1)$ from Equation (21) and the upper bound of $\sum_{i=2}^{i_{\max}} \mathbf{E}(h_i)$ using Equations (25) and (26), the upper bound of $\mathbf{E}(h)^c$ can be computed as:

$$\begin{aligned}\mathbf{E}(h)^c \le \frac{6P_0^c}{d_0^\alpha}\Bigg(\frac{6}{\pi}\int_{2}^{i_{\max}}\int_{0}^{\frac{\pi}{6}} \frac{r^2}{(\frac{r\cos(\frac{\pi}{6})}{\cos(\varphi)}+\beta)^\alpha}\, d\varphi\, dr \\ + \frac{(\alpha-2)^\alpha(2\sqrt{3}+\frac{4\pi}{3})}{3\beta^{\alpha-2}\alpha^\alpha} + \frac{1}{(1+\beta)^\alpha}\Bigg) \\ = \frac{6P_0}{d_0^\alpha}(\frac{6}{\pi}\int_{2}^{i_{\max}}\int_{0}^{\frac{\pi}{6}} \frac{r^2}{(\frac{r\cos(\frac{\pi}{6})}{\cos(\varphi)}+\beta)^\alpha}\, d\varphi\, dr + A(\alpha,\beta)).\end{aligned} \tag{27}$$

In Equation (27), we denote $A(\alpha,\beta)$ to $(\alpha-2)^\alpha(2\sqrt{3}+\frac{4\pi}{3})/(3\beta^{\alpha-2}\alpha^\alpha) + 1/(1+\beta)^\alpha$ that does not depend on the network size n.

Upper bound for expected hop count : Now, we determine the value of $i_{\max}$ to establish an upper bound for $\mathbf{E}(h)^c$. To compute $\mathbf{E}(h)^c$, we integrate the function

$$f(r,\varphi) = \frac{r^2}{(\frac{r\cos(\frac{\pi}{6})}{\cos(\varphi)} + \beta)^\alpha}$$

over the network area. It can be easily shown that for $r \gg \beta$, $f(r,\varphi) \propto 1/r^{\alpha-2}$, which implies that for $\alpha > 2$ and $r \gg 1$, the derivative satisfies

$$\frac{\partial f}{\partial r} < 0.$$

Under these conditions, by utilizing the network side length L defined in Equation (4) and as proven in Theorem 11, we approximate the network area with a circle of radius $R = L/\sqrt{\pi}$. Integrating over this circle provides an upper bound for $\mathbf{E}(h)^c$. Therefore, $i_{\max}$ is defined as

$$i_{\max} = \frac{L}{\sqrt{\pi} d_0} = \sqrt{\frac{\sqrt{3}n}{2\pi}}.$$

we can approximate the upper bound of the $\mathbf{E}(h)^c$. For $\alpha > 2$ and $\alpha \neq 3$, the integral over r could computed as and represented by $B(\varphi,\alpha,\beta,r)$ so that

$$B(\varphi,\alpha,\beta,r) = \int \frac{r^2}{(\frac{r\cos(\frac{\pi}{6})}{\cos(\varphi)} + \beta)^\alpha}\, dr = \frac{-\cos^3(\varphi)\begin{pmatrix}(\alpha-2)(\alpha-1)\sec^2(\varphi)\cos^2(\frac{\pi}{6})r^2 \\ +2(\alpha-1)\beta\sec(\varphi)\cos(\frac{\pi}{6})r\ +2\beta^2\end{pmatrix}}{(\sec(\varphi)\cos(\frac{\pi}{6})r+\beta)^{\alpha-1}(\alpha-3)(\alpha-2)(\alpha-1)\cos^3(\frac{\pi}{6})} + C_0. \quad (28)$$

Finally, by substituting P_0^c upper bound from Equation (17) the numerical upper bound values of $\mathbf{E}(h)^c$ for different α cases is achievable. The upper bound of $\mathbf{E}(h)^c$ for $\alpha \neq 3$ can be written as:

$$\mathbf{E}(h)^c \leq \frac{3\sqrt{3}}{2\pi(U(\alpha,\beta) - \frac{1}{3}(2W(\alpha,\beta,\sqrt{\frac{\sqrt{3}n}{8}}) + W(\alpha,\beta,\sqrt{\frac{n}{2\sqrt{3}}})))} \left[A(\alpha,\beta) + \frac{6}{\pi}\int_0^{\frac{\pi}{6}} \left| B(\varphi,\alpha,\beta,\sqrt{\frac{\sqrt{3}n}{2\pi}}) - B(\varphi,\alpha,\beta,2)\right| d\varphi\right]. \quad (29)$$

For $\alpha = 3$, the we represent the result of integral over r as $C(\varphi,\beta,r)$ that could be computed as

$$C(\varphi,\beta,r) = \int \frac{r^2}{(\frac{r\cos(\frac{\pi}{6})}{\cos(\varphi)} + \beta)^3}\, dr = \frac{2(\sec^2(\varphi)\cos^2(\frac{\pi}{6}) + \beta)\ln\left|\sec(\varphi)\cos(\frac{\pi}{6})r + \beta\right| + 4\beta\sec(\varphi)\cos(\frac{\pi}{6})r + 3\beta^2}{2(\sec(\varphi)\cos(\frac{\pi}{6})r+\beta)^2\sec^3(\varphi)\cos^3(\frac{\pi}{6})} + C_0. \quad (30)$$

Similarly, the numerical value can, for $\alpha = 3$ is expressed as:

$$\mathbf{E}(h)^c \leq \frac{3\sqrt{3}}{2\pi(U(3,\beta) - \frac{1}{3}(2W(\alpha,\beta,\sqrt{\frac{\sqrt{3}n}{8}}) + W(\alpha,\beta,\sqrt{\frac{n}{2\sqrt{3}}})))} \left[A(3,\beta) + \frac{6}{\pi}\int_0^{\frac{\pi}{6}} \left| C(\varphi,\beta,\sqrt{\frac{\sqrt{3}n}{2\pi}}) - C(\varphi,\beta,2)\right| d\varphi\right]. \quad (31)$$

If $\sqrt{n} \gg \beta$, which typically occurs in very large-scale distributed networks, and as shown in Section 6, where the typical value of β is around 10, $B(\varphi,\alpha,\beta,\sqrt{n\sqrt{3}/(2\pi)})$ simplifies to:

$$B(\varphi,\alpha,\beta,\sqrt{\frac{n\sqrt{3}}{2\pi}}) \approx \frac{\cos^\alpha(\varphi)\sec^\alpha(\frac{\pi}{6})}{(\alpha-3)(\frac{n\sqrt{3}}{2\pi})^{\frac{\alpha-3}{2}}}.$$

Considering the definition of W from Equation (B.24), could be easily shown that

$$\lim_{r \gg \beta} W(\alpha, \beta, r) = \frac{\alpha - 1}{r^{(\alpha-2)}}. \tag{32}$$

Thus, the final approximation for $\mathbf{E}(h)^c$ is:

$$\mathbf{E}(h)^c \leq \frac{3\sqrt{3}(\alpha-1)(\alpha-2)}{2\pi(U(\alpha,\beta) - \frac{(\alpha-1)}{3}(\frac{2}{\sqrt{\frac{\sqrt{3}n}{8}}} + \frac{1}{\sqrt{\frac{n}{2\sqrt{3}}}}))} \left[A(\alpha,\beta) + \left| B'(\alpha,\beta) - \frac{B''(\alpha)}{(\alpha-3)(\frac{n\sqrt{3}}{2\pi})^{\frac{\alpha-3}{2}}} \right| \right]. \tag{33}$$

where the value $B'(\alpha, \beta)$, are $B''(\alpha)$ are only rely on interaction probability parameters and not network size.

For $\alpha = 3$, substituting $A(3, \beta)$ and simplifying:

$$\mathbf{E}(h)^c \leq \frac{3\sqrt{3}(A'(3,\beta) + \frac{11\ln(\frac{3n}{2\pi})}{6\pi\sqrt{3}})}{2\pi(U(3,\beta) - \frac{2\sqrt{2}}{3\sqrt{n}}(\frac{1}{\sqrt[4]{3}} + \sqrt[4]{3}))}. \tag{34}$$

4.1.3 Analysis and numerical evaluation

The results presented in Equations (33) and (34) provide closed-form expressions for the upper bound of the expected hop count, $\mathbf{E}(h)$, in P2P connections within large-scale distributed networks. These findings are consistent with our previous work [24], which analyzed the asymptotic behavior of network capacity as $n \to \infty$. Specifically, both studies demonstrate that

$$\mathbf{E}(h) = \begin{cases} \Theta\left(n^{\frac{3-\alpha}{2}}\right), & \text{if } \alpha < 3, \\ \Theta(\ln n), & \text{if } \alpha = 3, \\ \Theta(1), & \text{if } \alpha > 3. \end{cases}$$

Numerical results in Figure 4, obtained for several values of α and β, use α–values drawn from real-world interaction–distance studies discussed in [24]. The figure illustrates the expected hop count across a wide range of network sizes on a logarithmic scale. The empirical curves align closely with the theoretical predictions for both $\alpha = 3$ and $\alpha \neq 3$, confirming the robustness of our analytic upper bound in capturing the relationship between network size, interaction probabilities, and hop distances. From a physical-intuition perspective, Figure 4 shows that for typical values of α and β, the expected hop count remains surprisingly small even for extremely large networks. For example, when $n = 10^8$, the network diameter is

$$\frac{L}{2d_0} = \sqrt[4]{3}\,\sqrt{n} \approx 13160$$

(see Equation (4)), whereas the expected hop count ranges only from 57 to 136, averaging around 100 hops across the tested α values and $\beta = 10$. This contrast underscores the dominant role of the interaction-probability model in determining network performance. The results further highlight the influence of the power-law exponent α, whose value significantly shapes the hop distribution and ultimately becomes a bottleneck for the scalability of large-scale distributed networks. The offset parameter β also plays an important role: differences in β reflect how real social-interaction data must be calibrated, and these differences noticeably shift the expected hop count.

Additionally, Figure 5 compares the analytic upper bound $E_{\text{an}}(h)^c$ with the discrete lattice computation $E_{\text{lat}}(h)^c$, both evaluated at the central node using symmetry. Across all β values, the true hop count is consistently about 10% lower than the analytic bound. This deviation arises almost entirely

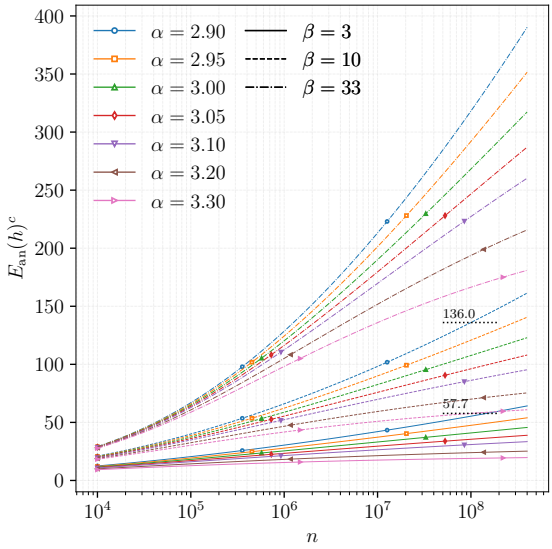

Figure 4: Analytic upper-bound estimates $E_{\mathrm{ub}}(h)^c$ of the expected hop count from the network center as a function of the network size n. Each curve corresponds to a different pair (α, β). For $n = 10^8$, the horizontal indicators mark the range of $E_{\mathrm{an}}(h)^c$ obtained across the considered values of α, showing that the expected hop count remains on the order of 10^2 even in ultra-large networks. In particular, for $\beta = 10$, the values of $E_{\mathrm{an}}(h)^c$ lie between 57 and 136.

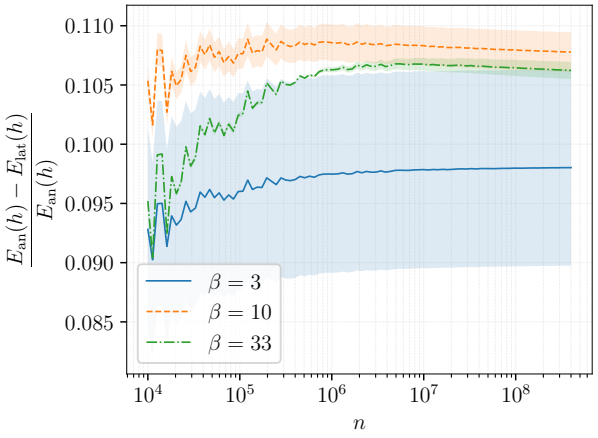

Figure 5: Relative deviation between the analytic upper-bound model and the lattice-based computation of the central-node hop count, $(E_{\mathrm{an}}(h)^c - E_{\mathrm{lat}}(h)^c)/E_{\mathrm{an}}(h)^c$. For each offset parameter β, the solid curve shows the mean deviation over all considered exponents α, while the shaded band indicates the corresponding standard deviation.

from the approximation of discrete ring summations by continuous integrals, with the largest discrepancy occurring in the innermost rings where the approximation is least precise. As expected, the standard deviation is largest for $\beta = 3$, since smaller offset values place greater weight on near-source nodes, amplifying the effect of early-ring approximation errors. Despite these small discrepancies, the approximation is sufficiently accurate for our purpose. First, it achieves the primary goal of providing the *first numerically tractable estimate* of the expected hop count in ultra-large networks. Second, the dominant source of sensitivity comes not from the upper-bound approximation but from the empirical uncertainty in α and β, which can change $\mathbf{E}(h)$ by factors—not by mere percentages. Third, since wireless topologies are inherently dynamic, extremely fine-grained precision is neither meaningful nor actionable for system design.

Most importantly, the results fundamentally reshape intuition: in a network that is 13,160 hops wide, the *average* communication path is roughly 100 hops—less than 1% of the network diameter. This reveals that large-scale distributed wireless networking can provide far shorter effective paths than previously assumed, dramatically improving the plausibility of scalable point-to-point capacity.

4.2 Average $\mathbf{E}(h)$ over the whole network

The previously derived value of $\mathbf{E}(h)$ applies only to a source node located at the network center. To extend the analysis to any node in the network, we consider a source positioned at polar coordinates (a, θ) with respect to the center, where

$$0 \le a \le \frac{\sqrt{2n}}{2}, \qquad 0 \le \theta < 2\pi,$$

as illustrated in Figure 6. In this general configuration, the maximum hop index $i_{\max}$ along each direction now depends on the source location (a, θ). Following the same reasoning used for the central-node case in Equation (12), the normalization condition for a general node becomes

$$\frac{2P_0(a,\theta)}{\sqrt{3}\, d_0^{\alpha}} \int_0^{2\pi} \sum_{i=1}^{i_{\max}(\vartheta|(a,\theta))} \frac{i}{\left(i + \frac{\beta_0}{d_0}\right)^{\alpha}} \, \mathrm{d}\vartheta = 1. \tag{35}$$

To make this computation tractable, we partition the angular domain $0 \le \vartheta < 2\pi$ into $K = 12$ sectors of width $\frac{\pi}{6}$, as shown in Figure 6. Within each sector k, the value of $i_{\max}(\vartheta \mid (a,\theta))$ is approximated by a constant $i_{\max}^k$. Substituting this approximation into Equation (35) gives

$$\frac{P_0(a,\theta)\,\pi}{3\sqrt{3} d_0^{\alpha}} \sum_{k=1}^{12} \sum_{i=1}^{i_{\max}^k} \frac{i}{\left(i + \frac{\beta_0}{d_0}\right)^{\alpha}} \approx 1.$$

Using the discrete-to-continuous approximation of Theorem 8, we rewrite this as

$$\frac{P_0(a,\theta)\,\pi}{3\sqrt{3} d_0^{\alpha}} \sum_{k=1}^{12} \left(\int_0^{i_{\max}^k} \frac{r}{(r+\beta)^{\alpha}} \, \mathrm{d}r - \frac{(\alpha-1)^{\alpha-1}}{\alpha^{\alpha}\beta^{\alpha-1}} \right) \le 1.$$

The integral term represents the continuous approximation of the hop contributions in each sector. Using the closed-form expressions $U(\alpha,\beta)$ and $W(r_k,\alpha,\beta)$ from Equations (16) and (B.24), we define the sector contribution function

$$F(r_k) = \frac{\pi}{3\sqrt{3}\, d_0^{\alpha}} \left(U(\alpha,\beta) - W(r_k,\alpha,\beta) \right), \tag{36}$$

where r_k^s is the radial extent needed to cover the network boundary within sector k. Thus, the resulting upper bound for the normalization constant at an arbitrary node is

$$P_0(a,\theta) \le \frac{1}{\sum_{k=1}^{12} F(r_k^s)}.$$

This formulation generalizes the computation of P_0 to all possible node positions in the network and enables the evaluation of the average hop count $\mathbf{E}(h)$ over the entire network area.

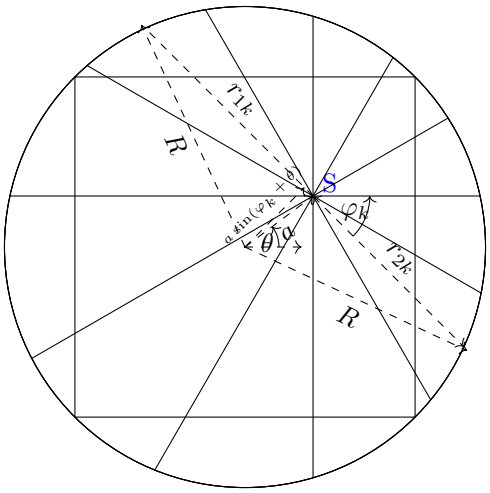

Figure 6: Network sectoring for a general source node position. The source node S is located at the polar position (a, θ) with respect to the network center. Relative to S, the network can be divided into 6 pairs of sectors with radii (r_{1k}, r_{2k}).

4.2.1 Convex optimization and geometric analysis for determining extreme values of P_0

To study the extremal values of $P_0(a, \theta)$, we examine the dependence of the sector contribution $F(r_k)$ on the radial extent r_k. For $\alpha > 2$ and $r_k > 1$, one can verify that

$$\frac{\partial U}{\partial r_k} = 0, \qquad \frac{\partial(-W)}{\partial r_k} < 0, \qquad \frac{\partial^2(-W)}{\partial r_k^2} < 0,$$

so that $F(r_k)$ is a strictly decreasing and concave function of r_k. Intuitively, sectors that extend farther from the source contribute less to the normalization sum, while shorter sectors contribute more. To obtain a tractable geometric bound, we first embed the square network in a circle of radius

$$R = \frac{\sqrt[4]{3}}{2}\, d_0 \sqrt{n}$$

and extend each sector until it intersects this circle. Let r_k denote the resulting radial extent in sector k for a given source location (a, θ). The geometry of the construction implies the quadratic constraint

$$\sum_{k=1}^{12} r_k^2 = 12R^2.$$

Because $F(\cdot)$ is concave in r (and, equivalently, in r^2), the sum $\sum_{k=1}^{12} F(r_k)$ is maximized when all radii are equal. By symmetry of the circular embedding, this happens when the source is at the center, in which case $r_k = R$ for all k, and hence

$$\sum_{k=1}^{12} F(r_k) \le 12\, F(R),$$

with equality if and only if the source is located at the center. In the actual square network, the effective radial lengths r_k^s in each sector are never larger than those of the encompassing circle, i.e., $r_k^s \le r_k$ for all k. Since F is decreasing, this implies

$$F(r_k^s) \ge F(r_k), \qquad \text{for all } k,$$

and thus

$$\sum_{k=1}^{12} F(r_k^s) \ge \sum_{k=1}^{12} F(r_k) \text{ for any source position } (a, \theta).$$

Combining these observations, we obtain the bound

$$\sum_{k=1}^{12} F(r_k^s) \geq 12\, F(R),$$

and therefore, from $P_0(a,\theta) \leq 1/\left(\sum_{k=1}^{12} F(r_k^s)\right)$, we see that

$$P_0(a,\theta) \leq \frac{1}{12\, F(R)},$$

with equality at the network center. In other words, the central node attains the smallest normalization constant P_0, while nodes away from the center yield larger values of P_0. This is consistent with the intuition that a centrally located node experiences the largest aggregate interaction weight and therefore requires the smallest normalization factor.

In contrast, the maximum P_0 value occurs at the network corners, where only three sectors (each with $r_k \leq 2R$) cover all nodes. Since the number of nodes per ring is reduced to $\frac{\pi}{2}i$ rather than $2\pi i$, the maximum value of P_0 is calculated as:

$$\lim_{\sqrt{n}\to\infty} P_0^{\max} \leq \frac{\sqrt{3}d_0^{\alpha}(\alpha-1)(\alpha-2)}{\pi(U(\alpha,\beta) - W(\sqrt{\frac{n}{\pi}},\alpha,\beta))} = \frac{\sqrt{3}d_0^{\alpha}(\alpha-1)(\alpha-2)}{\pi U(\alpha,\beta)} = 4P_0^{\min}. \tag{37}$$

This indicates that $P_0^{\max}$ is approximately four times greater than $P_0^{\min}$, calculated for the center node. More precisely, there are three $\frac{\pi}{6}$ sectors instead of 12, with two sectors bounded by $2\sqrt{n/3}$ and one by $\sqrt{2n}$.

4.2.2 P_0 distribution: Rapid convergence to the central value from network corners

Here, we examine the behavior of P_0 for nodes located well within the network, sufficiently distant from the edges such that their distance from all boundaries is at least $\kappa\beta$. While the maximum value of P_0 is observed at the network corners, our primary focus is on its behavior as the position shifts from a corner toward the center along the diagonal line $x = y$. We denote P_0 at a distance $\kappa\beta$ from all boundaries as $P_0^{\kappa\beta}$. To quantify this behavior, we calculate the ratio $P_0^{\min}/P_0^{\kappa\beta}$, as detailed in Theorem 10:

$$\frac{P_0^{\min}}{P_0^{\kappa\beta}} \geq \begin{cases} 1 - \frac{1+\frac{1}{\pi}}{\kappa+1}, & \text{if } \alpha \geq 3 \\ 1 - \frac{0.75\alpha - 1.25 + \frac{1}{\pi}}{(\kappa+1)^{\alpha-2}}, & \text{if } \alpha \approx 3 \end{cases}$$

For both cases, as $\kappa \gg 1$:

$$\lim_{\kappa\gg 1} \frac{P_0^{\min}}{P_0^{\kappa\beta}} = 1$$

This result indicates that for nodes located at least $\kappa\beta$ hops away from any network boundary, P_0 can be effectively approximated by $P_0^{\min}$. Despite P_0 being four times larger at the network corners than its central value, $P_0^{\min}$, the rapid convergence ensures that P_0 for most nodes in the network closely matches the value at the center.

4.2.3 Global maximum of $\mathbf{E}(h)$ at the network center (except near corners)

The expression derived in Equation (27) gives the expected hop count $\mathbf{E}(h)^c$ for a source node located at the network center, obtained by dividing the network into 12 symmetric sectors in which the maximum hop count $i_{\max}$ is identical across all sectors. Thus, each sector contributes exactly one–twelfth of the total value $\mathbf{E}(h)^c$. For a source node located at an arbitrary position (a,θ), this symmetry no longer

holds: the maximum hop count in each sector, denoted $i^k_{\max}$, differs with k. The hop-count expression can therefore be generalized as

$$\mathbf{E}(h)(a,\theta) \le \frac{P_0(a,\theta)}{d_0^\alpha} \sum_{k=1}^{12} \left(\frac{3}{\pi} \int_2^{i^k_{\max}} \int_0^{\frac{\pi}{6}} \frac{r^2}{\left(\frac{r\cos(\pi/6)}{\cos\varphi} + \beta\right)^\alpha} \,\mathrm{d}\varphi \,\mathrm{d}r + \frac{A(\alpha,\beta)}{2} \right). \tag{38}$$

For all nodes away from the four corner regions, the normalization factor satisfies $P_0(a,\theta) \approx P_0^{\min}$, as shown previously. Define the sector contribution

$$G(r_k) = \frac{3}{\pi d_0^\alpha} \left(\int_2^{r_k} \int_0^{\pi/6} \frac{r^2}{\left(\frac{r\cos(\pi/6)}{\cos\varphi} + \beta\right)^\alpha} \,\mathrm{d}\varphi \,\mathrm{d}r + \frac{\pi A(\alpha,\beta)}{2} \right). \tag{39}$$

Using this notation, and writing r_k^s for the radial extent of sector k required to cover the network area, we obtain the bound

$$\mathbf{E}(h)(a,\theta) \le P_0^{\min} \sum_{k=1}^{12} G(r_k^s).$$

For $\alpha > 2$, the function $G(r)$ is strictly decreasing and concave for $r > 1$. As in the analysis of $P_0(a,\theta)$, geometric symmetry implies that the radii $\{r_k\}$ satisfy the quadratic constraint

$$\sum_{k=1}^{12} (r_k^s)^2 = 12R^2,$$

where R is the radius of the smallest circle enclosing the square network. Because G is concave, the sum $\sum_{k=1}^{12} G(r_k^s)$ is maximized when all r_k^s are equal, i.e., $r_k^s = R$ for all k, which occurs when the source node is exactly at the center of the network. Thus, the expected hop count is maximized at the network center:

$$\mathbf{E}(h)(a,\theta) \le P_0^{\min} \sum_{k=1}^{12} G(R) = \frac{G(R)}{F(R)} = \mathbf{E}(h)^c,$$

where $\mathbf{E}(h)^c$ denotes the analytic value derived for a source at the center. Except for nodes located in small regions near the network corners (where normalization effects dominate), $\mathbf{E}(h)^c$ therefore represents the global maximum of the expected hop count over the entire network.

Conclusion: The central-node value $\mathbf{E}(h)^c$ as an upper bound for the network-wide average

We now show that the expected hop count averaged over all nodes in the network converges to the central-node value $\mathbf{E}(h)^c$ as the network grows. This establishes $\mathbf{E}(h)^c$ as an asymptotically tight upper bound for the network-wide average $\mathbf{E}(h)$. For all nodes whose distance from every network boundary exceeds $\kappa\beta$, the normalization constant satisfies $P_0(a,\theta) \approx P_0^{\min}$, and the sector radii satisfy the same geometric constraints as those of the central node. From the concavity analysis in the previous subsection, these nodes satisfy

$$\mathbf{E}(h)(a,\theta) \le \mathbf{E}(h)^c, \quad \text{except a vanishing fraction of nodes.}$$

The total number of nodes located within distance $\kappa\beta$ of the network boundary is

$$N_{\text{bdry}} \approx 2\kappa\beta\sqrt{n} + \kappa^2\beta^2,$$

whereas the remaining $n - N_{\text{bdry}}$ interior nodes have hop count at most $\mathbf{E}(h)^c$. Hence the average satisfies

$$\mathbf{E}(h) \le \frac{(\sqrt{n} - \kappa\beta)^2 \, \mathbf{E}(h)^c + (2\kappa\beta\sqrt{n} + \kappa^2\beta^2) \, \mathbf{E}(h)_{\max}}{n},$$

where $\mathbf{E}(h)_{\max}$ is the value obtained at the network corner. Since β is constant and $\sqrt{n} \gg \kappa\beta$, taking the limit gives

$$\lim_{n\to\infty} \mathbf{E}(h) = \lim_{n\to\infty} \left(\left(1 - \tfrac{2\kappa\beta}{\sqrt{n}}\right)\mathbf{E}(h)^c + \tfrac{2\kappa\beta}{\sqrt{n}}\mathbf{E}(h)_{\max} \right) = \mathbf{E}(h)^c.$$

Although the expected hop count achieves its maximum at the corners of the network, their contribution to the average vanishes as $n \to \infty$. For completeness, closed-form expressions for $\mathbf{E}(h)_{\max}$ at the corner are given in Equation (40) for $\alpha = 3$ and Equation (41) for $\alpha \neq 3$.

$$\mathbf{E}(h) = \frac{3\sqrt{3}}{\pi(U(3,\beta) - \frac{4}{3\sqrt{\frac{n}{3}}} - \frac{2}{3\sqrt{\frac{n}{2}}})} \left[A'(\beta) + \frac{22\ln(3n)}{\pi 9\sqrt{3}} + \frac{11\ln(4n)}{\pi 9\sqrt{3}} \right]. \tag{40}$$

$$\mathbf{E}(h) = \frac{3\sqrt{3}(\alpha-1)(\alpha-2)}{\pi(U(\alpha,\beta) - \frac{2(\alpha-1)}{3(\sqrt{\frac{n}{3}})^{\alpha-2}} - \frac{(\alpha-1)}{3(\sqrt{\frac{n}{2}})^{\alpha-2}})} \left[A(\alpha,\beta) + \left| B'(\alpha,\beta) - \frac{B''(\alpha)}{3(\alpha-3)} \left(\frac{2}{(\frac{4n}{3})^{\frac{\alpha-3}{2}}} + \frac{1}{(2n)^{\frac{\alpha-3}{2}}} \right) \right| \right]. \tag{41}$$

These formulas confirm that $\mathbf{E}(h)_{\max}$ exceeds $\mathbf{E}(h)^c$ by only a constant factor. Thus, for all $\alpha \geq 2.5$, the central-node value $\mathbf{E}(h)^c$ serves as the global upper bound for $\mathbf{E}(h)$ over almost all nodes and equals the network-wide average in the limit $n \to \infty$.

4.3 $\mathbf{E}(h)$ distribution across the network and numerical validation

To validate the analytical results and to understand how the expected hop count varies across the entire network area, we compute and visualize the spatial distribution of the upper bound of $\mathbf{E}(h)$ for both disk- and square-shaped networks. Our goal is not to obtain the exact value of $\mathbf{E}(h)$ for each node, but rather to examine how the analytically derived upper bound behaves across the domain and to confirm that the central-node value $\mathbf{E}(h)^c$ indeed acts as a tight upper bound for almost all nodes. For any node at position (a, θ) relative to the network center, the expected hop count can be approximated using the sector-based decomposition developed earlier:

$$\mathbf{E}(h \mid a, \theta) \approx \frac{\sum_{k=1}^{12} G(r_k(a,\theta))}{\sum_{k=1}^{12} F(r_k(a,\theta))},$$

where $F(\cdot)$ and $G(\cdot)$ are defined in Equations (36) and (39). The quantities $r_k(a,\theta)$ denote the sector radii determined by geometry. For a disk-shaped network of radius $R = \sqrt{n/\pi}$, this yields

$$r_k(a,\theta) = \sqrt{R^2 + a^2\left(\frac{\cos^2(\theta+\varphi_k)}{4} - 1\right)} \pm \frac{a\cos(\theta+\varphi_k)}{2},$$

with $\varphi_k = (k-1)\pi/6$, $0 \leq a \leq R$, and $0 \leq \theta < 2\pi$.

The disk geometry allows evaluating the upper bound uniformly over all possible node positions. As illustrated in Figure 7, the central value $\mathbf{E}(h)^c$ is the global maximum for almost the entire domain. The expected hop count decreases toward the edge of the disk, reaching its minimum near the boundary. This confirms the analytical conclusion that the central-node value forms an upper bound for the network-wide average when $\alpha > 2$, because local interactions dominate and distant nodes contribute weakly to hop count.

For square networks, the interior region behaves similarly to the disk case: nodes sufficiently far from the boundary satisfy $\mathbf{E}(h \mid x, y) \approx \mathbf{E}(h)^c$. Near the boundary, however, the hop count exhibits directional variation. To visualize these effects, Figure 8 plots $\mathbf{E}(h)$ along the most informative boundary directions: the diagonal ($x = y$) and the vertical/horizontal edges ($x = L$ or $y = L$). Along these lines, $\mathbf{E}(h)$ first decreases as one approaches the edge, then increases sharply near the corners, where the longest radii appear.

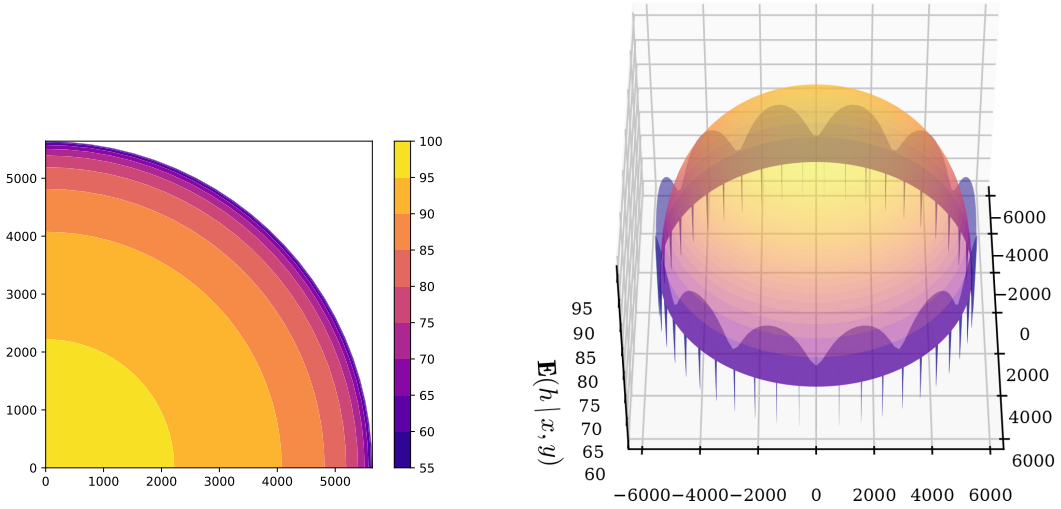

Figure 7: Numerical upper-bound approximation of $\mathbf{E}(h \mid x, y)$ for a disk network with $n = 10^8$, $\alpha = 3.05$, and $\beta = 10$. The central node exhibits the highest expected hop count, confirming that $\mathbf{E}(h)^c$ upper-bounds the values for almost all nodes.

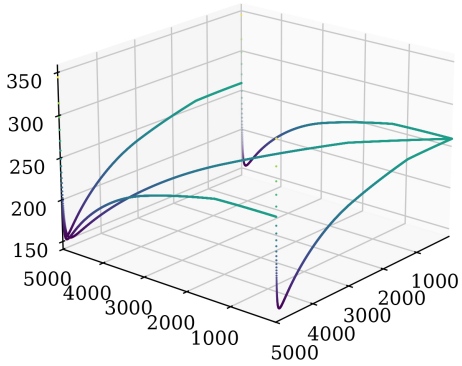

Figure 8: Upper-bound approximation of $\mathbf{E}(h \mid x, y)$ for a square network with $n = 10^8$, $\alpha = 2.65$, and $\beta = 10$. The value decreases from the center toward the boundary and rises sharply near the corners.

A common intuition is that nodes near the center of the network should have smaller expected hop counts because they are closer, on average, to other nodes. Our analysis shows the opposite: the center exhibits the larges expected hop count, and therefore forms the global upper bound for $\mathbf{E}(h)$ over almost the entire network. The reason is the power-law interaction model with $\alpha > 2$. Most communication events occur locally; distant nodes contribute marginal probability mass. A node at the center is surrounded symmetrically by the largest total number of nodes at all distances, and the cumulative effect of long-distance contributions—though individually small—accumulates more at the center than at any other location. Nodes away from the center have a truncated far-field region, reducing the total expected hop count compared to the center. Because $\mathbf{E}(h)^c$ serves as a tight upper bound for nearly all nodes, we use this value in the numerical performance evaluation as the "worst-case representative" for the expected hop count. For square networks, the diagonal profile of $\mathbf{E}(h)(x, y)$ along the line $x = y$, shown in Figure 8, provides a tight upper bound. Specifically, for any $x = a$, the value $\mathbf{E}(h)(x, y)|_{x=y=a}$ upper-bounds the average hop count over a thin square of side length $\sqrt{2}\,a$ centered at the network center. By taking a weighted average of $a\,\mathbf{E}(h)(x, y)|_{x=y=a}$ as a varies from the center to the network corner, we obtain a bound that is tighter than $\mathbf{E}(h)^c$.This refined bound is used to improve the numerical results reported in Section 6.

Overall, the numerical evidence strongly supports the analytical conclusion: the hop-count distribution is sharply peaked around the central-node value, and $\mathbf{E}(h)^c$ is a reliable upper bound for almost all network nodes.

5 Expected transmission capacity

In this section, we compute the expected transmission rate per node, denoted $\mathbf{E}(C_{\text{eff}})$, under the assumption that all nodes use identical wireless technologies and experience uniform attenuation throughout the network. The symmetric network topology is illustrated in Figure 9. For a given node density ρ, the total network area is $\frac{n}{\rho}$. In this scenario, we assume that all available frequency resources may be reused by any active link; hence, all simultaneously active links share the entire spectrum through spatial reuse. To control cross-interference, each active link is allocated a reserved spatial region of area proportional to $(1+\Delta)^2$, where $\Delta > 1$ is the space-reservation parameter (analogous to protocol-model guard zones, but not based on circular exclusion regions). As shown in Figure 9, each active link with length $r = d_0$ occupies an area

$$\frac{(1+\Delta)^2}{\rho} = \frac{\sqrt{3}}{2} r^2 (1+\Delta)^2.$$

Thus, only one active link may exist within each such reserved region. The practical implementation may rely on RTS/CTS signaling or a distributed TDMA scheduler. However, our objective here is not to model the MAC protocol itself, but rather to characterize the *maximum possible* transmission capacity under ideal spatial reuse. Let b_t denote the total concurrent transmission rate at time t. If $n_L(t)$ links are active and each link has instantaneous rate $C_L^i(t)$, then

$$b_t = \sum_{i=1}^{n_L(t)} C_L^i(t).$$

Assuming ergodicity, so that time averages equal ensemble averages, we obtain

$$\mathbf{E}(b) = \mathbf{E}\left(\sum_{i=1}^{n_L} C_L^i\right) = \sum_{i=1}^{n_L} \mathbf{E}(C_L^i) = \mathbf{E}(n_L)\,\mathbf{E}(C_L). \tag{42}$$

Here, $\mathbf{E}(n_L)$ represents the *spatial reuse factor*, i.e., the expected number of links that can be active simultaneously. The maximum spatial reuse is achieved when the entire network area is fully covered with non-overlapping reserved regions. In that case,

$$\mathbf{E}(n_L) \leq \frac{\text{Total Network Area}}{\text{Area per Link}} = \frac{\frac{n}{\rho}}{\frac{(1+\Delta)^2}{\rho}} = \frac{n}{(1+\Delta)^2}. \tag{43}$$

This upper bound may not always be achievable due to suboptimal scheduling or an uneven distribution of nodes with buffered data. Nevertheless, in this work we adopt it as an upper bound on the total transmission capacity, providing a reference against which distributed network performance may be evaluated.

The effective per-node capacity, denoted $\mathbf{E}(C_{\text{eff}})$, represents the maximum average transmission rate that each node can sustain continuously. Using Equation (42) and dividing the total rate by n, we obtain

$$\mathbf{E}(C_{\text{eff}}) = \frac{\mathbf{E}(b)}{n} = \frac{\mathbf{E}(n_L)\,\mathbf{E}(C_L)}{n} = \frac{\mathbf{E}(C_L)}{(1+\Delta)^2}. \tag{44}$$

This expression is consistent with the general formulation in Equation (2), where the effective reserved area per link, $\mathbf{E}(A_\rho)$, equals $(1+\Delta)^2$ in this symmetric setting. In other words, each active transmission consumes an area $(1+\Delta)^2$ times the node density.

Communication model: In the symmetric arrangement considered in this work, such as the hexagonal lattice shown in Figure 9, all active links operate in the same frequency band f and have identical link lengths r. Since our objective is to maximize the number of simultaneous transmitters, the network operates in an *interference-limited* regime, where aggregate interference—rather than thermal noise—dominates the received signal quality.In this work we focus on the large-scale behavior of distributed wireless networks, where the dominant factors shaping interference are the geometric arrangement of nodes and the classical path-loss model. Since all transmitters experience statistically identical fading, the expected SINR is determined primarily by distance attenuation, and incorporating fading into the analytical interference derivation provides little additional structural insight while greatly complicating the closed-form expressions. For this reason, we omit fading in the analytical model and characterize interference using only path-loss and geometry. However, to capture the exact achievable throughput, our simulations incorporate a full channel model—including path-loss, lognormal shadowing, and Rayleigh small-scale fading—applied to every interfering distance derived from the analytical geometry. This ensures that while the theory describes the fundamental large-scale behavior, the simulation reflects the true upper bound on network throughput under realistic wireless channels.

All nodes employ identical antenna characteristics, with receiving gain g_r and transmitting gain g_t, and the medium exhibits uniform attenuation with path-loss exponent α_p. The received power at distance r is therefore

$$P_r = \frac{P_t(4\pi f)^2 g_r g_t}{c^2 r^{\alpha_p}} = \frac{P_t g_0}{r^{\alpha_p}}, \tag{45}$$

where c is the speed of light, P_t is the transmission power, and $g_0 = (4\pi f)^2 g_r g_t / c^2$ represents the overall gain parameter.

Given the uniformity in transmitter and receiver characteristics and the homogeneous propagation environment, all nodes use the same transmission power $P_t = P$. Since the network is interference-limited, equalizing the transmit power across all nodes ensures fair spatial reuse and avoids biasing the interference field. Accordingly, the received power for any transmitter–receiver pair at distance r simplifies to:

$$P_r = \frac{P g_0}{r^{\alpha_p}}. \tag{46}$$

For any link L, the Shannon capacity C_L is calculated as:

$$C_L = W \log_2(1 + \text{SINR}), \tag{47}$$

where W is the channel bandwidth and SINR denotes the Signal-to-Interference-plus-Noise Ratio at the receiver. Since all links operate over the same bandwidth W, evaluating the SINR is sufficient to determine the link rate C_L. Furthermore, in our symmetric setting the received signal power S is identical across all active links because they share the same link length, antenna gains, and transmission power. Hence, differences in link capacity arise solely from variations in the interference power I. Therefore, to characterize C_L, it suffices to compute the interference level at each receiver, which we derive in the following subsection.

5.0.1 Computing the upper bound of cross-interference

We focus on the receiving node of the central link in the network. The interference experienced by this node comes from all other active transmitters in the network. Given the symmetric topology and uniform parameters, we can compute an upper bound of the cross-interference I by summing the contributions from all interfering transmitters. The interference power from a single interfering transmitter at a distance d is:

$$I(d) = \frac{P g_0}{d^{\alpha_p}}. \tag{48}$$

The total interference I is then the sum over all interfering transmitters:

$$I = \sum_{i \neq 0} \frac{P g_0}{d_i^{\alpha_p}}, \tag{49}$$

where d_i is the distance from the interfering transmitter i to the receiver of the central link.

To compute the upper bound, we consider the closest possible arrangement of interfering transmitters, which occurs when they are placed at the minimum allowable distance determined by Δ. By integrating over the network area and considering the spatial distribution of interfering nodes, we can derive an expression for I as a function of Δ and α_p.

5.0.2 Approximating the average cross-interference

Due to the symmetry and uniformity of the network, the interference experienced by a centrally located receiver serves as an upper bound for all other nodes. Moreover, the average interference at any receiver converges to the value computed for the central link as the network grows. This property allows the interference upper bound to be generalized to all network nodes, significantly simplifying the analysis.

5.0.3 Computing and maximizing $\mathbf{E}(C_{\text{eff}})$

With the expressions for S and I after regulating transmitting power , we can compute the SINR:

$$\text{SINR} = \frac{S}{I + N_0}, \tag{50}$$

where N_0 is the noise power. Substituting S and I into the Shannon capacity formula (47), we obtain $\mathbf{E}(C_L)$ as a function of Δ and α_p. Finally, we aim to maximize $\mathbf{E}(C_{\text{eff}})$ with respect to Δ:

$$\mathbf{E}(C_{\text{eff}}) = \frac{\mathbf{E}(C_L)}{(1+\Delta)^2} \quad \text{maximize over } \Delta. \tag{51}$$

A larger Δ results in a greater Signal-to-Interference-plus-Noise Ratio (SINR) and higher link capacity for active links but reduces the number of concurrent links. Therefore, we can determine the optimal Δ_{opt} that yields the maximum expected transmission rate per node.

5.1 Calculation of total interference at the central receiver

The interference I experienced by a receiver depends on its location within the network. For a receiver situated at the network center, interference arrives uniformly from all directions due to the network's symmetry. In our scenario, transmitter-receiver pairs are arranged in a regular hexagonal lattice, as illustrated in Figure 9. To limit cross-interference, each link reserves a hexagonal area of $\sqrt{3}(1+\Delta)^2 r^2/2$, centered at the midpoint between the transmitter and receiver.

Because nodes equidistant from the receiver contribute equally to the interference, we group interfering nodes into nested hexagonal rings based on their distances from the receiver. Let $I(i)$ denote the total interference from the i^{th} ring of active transmitters. Therefore, the total interference at the central receiver is given by

$$I = \sum_{i=1}^{i_{\max}} I(i). \tag{52}$$

In each i^{th} ring surrounding the central link, there are $6i$ interfering transmitters, as shown in Figure 11. Each sector k (where $1 \leq k \leq 6$) contains i transmitter-receiver pairs. The distance between an interfering transmitter j (with $1 \leq j \leq i$) and the receiver varies slightly with the angle φ_j. Here, φ_j

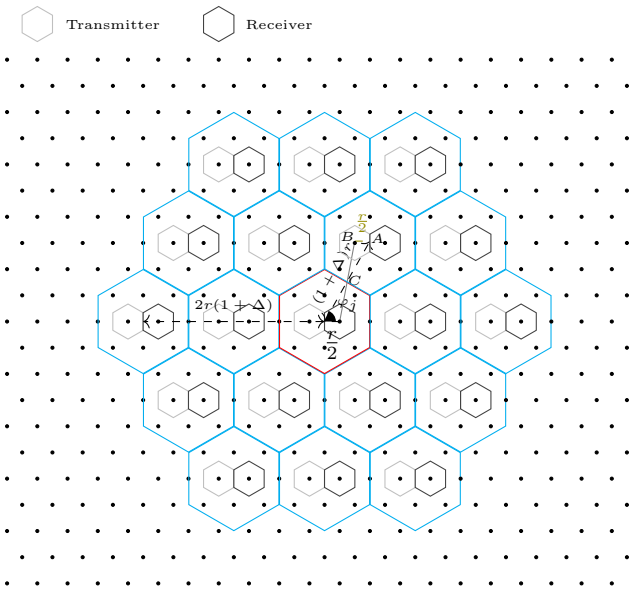

Figure 9: Symmetric arrangement of transmitter–receiver pairs in a hexagonal lattice. Each link has identical length r and operates under the same transmission power and antenna characteristics. The shaded hexagons illustrate the spatial reuse pattern, where only one transmitter–receiver pair is activated per a reservation region. The highlighted central link and its surrounding interferers define the geometric structure used to compute the interference at the receiver. $r(\varphi_j)$ appearing in the interference expression are derived from the local geometry shown in Figure 10.

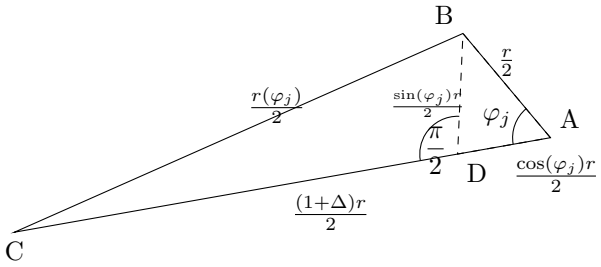

Figure 10: Local geometry used to calculate the distance from the receiver of the central link to an interferer located in the first ring of the hexagonal lattice. Given that all link lengths are r, the triangle (A, B, C) relates the reserved-space parameter Δ and the angular offset φ_j to the actual positions of interfering nodes. The auxiliary point D allows closed-form derivation for $r(\varphi_j)$ used in the interference computation.

represents the angle between the sector's perpendicular bisector and the line connecting the bisector of the central receiver-transmitter pair to that of the j^{th} receiver-transmitter pair within the same sector. In the first ring ($i = 1$), six interfering transmitters are located at angles $\varphi_j \in \{0, \pi/3, \ldots, 5\pi/3\}$.

To calculate the distances to the interfering nodes, we refer to Figure 10, which shows a magnified view of triangle $\triangle ABC$ from Figure 9. In this triangle, $r(\varphi_j)/2 = \overline{BC}$, and $r(\varphi_j)$ is expressed as

$$\begin{aligned} r(\varphi_j) = 2\overline{BC} &= \sqrt{(\overline{AC} - \overline{DC})^2 + \overline{BD}^2} \\ &= 2\sqrt{(\frac{(1+\Delta)r}{2} - \frac{r}{2}\cos(\varphi_j))^2 + (\frac{r}{2}\sin(\varphi_j))^2} \\ &= r\sqrt{(1+\Delta-\cos(\varphi_j))^2 + (\sin(\varphi_j))^2}\,, \end{aligned}$$

which leads to the interference power from transmitter j being

$$I(1,j) = \frac{Pg_0}{r^{\alpha_p}((1+\Delta-\cos(\varphi_j))^2 + (\sin(\varphi_j))^2)^{\frac{\alpha_p}{2}}}. \tag{53}$$

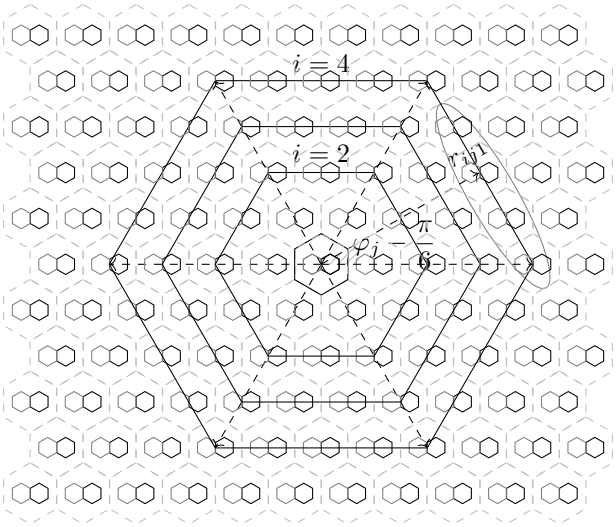

Figure 11: Illustration of the interfering transmitters surrounding the central link and the sectorization of each interference ring in the hexagonal lattice. Concentric hexagons represent successive rings ($i = 2, 4, \ldots$), and each ring is partitioned into 6 identical sectors. The dashed arrows indicate the distances r_{ij1} from the receiver of the central link to representative interferers in each ring. The shaded elliptical region highlights the range of angular deviations ($\varphi_j - \frac{\pi}{6}$) arising from the geometric offset of the hexagonal grid. This sectorized structure is used to derive closed-form expressions for the interference contributed by each ring in the analytical model.

Thus, the total interference from the first ring is given by

$$I(1) = \sum_{j=1}^{6} \frac{Pg_0}{r(\varphi_j)^{\alpha_p}} = \frac{Pg_0}{r^{\alpha_p}} \sum_{j=1}^{6} \frac{1}{\xi(\Delta, \varphi_j)^{\alpha_p}}, \tag{54}$$

where P is the transmission power, g_0 is the overall gain parameter, α_p is the path loss exponent, and $\xi(\Delta, \varphi_j)$ is defined as

$$\xi(\Delta, \varphi_j) = \sqrt{[(1+\Delta) - \cos(\varphi_j)]^2 + \sin^2(\varphi_j)}. \tag{55}$$

For rings with $i \geq 2$, each ring is divided into six identical sectors, each containing i transmitters. According to Theorem 3, the distance from the receiver to an interfering transmitter in ring i, sector k, at angle φ_j is given by

$$r_{ijk} = r\,\psi(i, \varphi_j, k), \tag{56}$$

with

$$\psi(i, \varphi_j, k) = \left[\left(\frac{i(1+\Delta)\cos\left(\frac{\pi}{6}\right)}{\cos\left(\varphi_j - \frac{\pi}{6}\right)} - \cos\left(\varphi_j + \frac{(k-1)\pi}{3}\right) \right)^2 + \sin^2\left(\varphi_j + \frac{(k-1)\pi}{3}\right) \right]^{\frac{1}{2}}. \tag{57}$$

Therefore, the total interference from ring i is

$$I(i) = \sum_{k=1}^{6} \sum_{j=1}^{i} \frac{Pg_0}{r_{ijk}^{\alpha_p}} = \frac{Pg_0}{r^{\alpha_p}} \sum_{k=1}^{6} \sum_{j=1}^{i} \frac{1}{(\psi(i, \varphi_j, k))^{\alpha_p}}. \tag{58}$$

Combining the contributions from all rings, the cumulative interference at the central receiver is

$$I = I(1) + \sum_{i=2}^{i_{\max}} I(i) = \frac{Pg_0}{r^{\alpha_p}} \left[\sum_{j=1}^{6} \frac{1}{(\xi(\Delta, \varphi_j))^{\alpha_p}} + \sum_{i=2}^{i_{\max}} \sum_{k=1}^{6} \sum_{j=1}^{i} \frac{1}{(\psi(i, \varphi_j, k))^{\alpha_p}} \right]. \tag{59}$$

To simplify and bound the interference from distant rings ($i > \kappa/1+\Delta$), we introduce the function $\chi(\Delta, \alpha_p, \kappa)$, which aggregates the interference contributions beyond a certain threshold κ with:

$$\chi(\Delta, \alpha_p, \kappa, C_k) = \frac{Q(\alpha_p)(1+\Delta)^{-1}(\alpha_p - 1)(\left\lceil \frac{\kappa}{1+\Delta} \right\rceil - 0.5) - C_k(1+\Delta)^{-2}}{\left[(1+\Delta)(\left\lceil \frac{\kappa}{1+\Delta} \right\rceil - 0.5) - C_k\right]^{\alpha_p - 1} (\alpha_p - 2)(\alpha_p - 1)}. \tag{60}$$

where C_k are constants that ensure upper interference upper bound specific to each sector k provided in Table A.1, and $Q(\alpha_p) = \int_0^{\frac{\pi}{3}} \frac{\cos^{\alpha_p}(\varphi - \frac{\pi}{6})}{\cos^{\alpha_p}(\frac{\pi}{6})} d\varphi$.

The detailed expression for $\chi(\Delta, \alpha_p, \kappa)$ and the derivation process are provided in Theorem 5. Then, the upper bound of the total interference is then expressed as

$$I \leq \frac{Pg_0}{r^{\alpha_p}} [\sum_{j=1}^{6} \frac{1}{(\xi(\Delta, \varphi_j))^{\alpha_p}} + \sum_{i=2}^{\left\lfloor \frac{\kappa}{1+\Delta} \right\rfloor} \sum_{k=1}^{6} \sum_{j=1}^{i} \frac{1}{(\psi(i, \varphi_j, k))^{\alpha_p}} + \frac{3}{\pi} \sum_{k=1}^{6} \chi(\Delta, \alpha_p, \kappa)]. \tag{61}$$

Here, $f(\Delta, \alpha_p)$ represents the total interference function and is defined as

$$f(\Delta, \alpha_p) = \sum_{j=1}^{6} \frac{1}{(\xi(\Delta, \varphi_j))^{\alpha_p}} + \frac{3}{\pi} \sum_{k=1}^{6} \chi(\Delta, \alpha_p, \kappa) + \sum_{i=2}^{\left\lfloor \frac{\kappa}{1+\Delta} \right\rfloor} \sum_{k=1}^{6} \sum_{j=1}^{i} \frac{1}{(\psi(i, \varphi_j, k))^{\alpha_p}}. \tag{62}$$

Thus, the upper bound of the total interference can be succinctly expressed as

$$I \leq \frac{Pg_0}{r^{\alpha_p}} f(\Delta, \alpha_p). \tag{63}$$

This expression provides a manageable way to estimate the total interference at the central receiver, accounting for both the contributions from nearby rings and the bounded interference from distant rings.

5.2 Average cross-interference approaching the upper bound

We first derived an upper bound on the interference experienced by a receiver located at the center of the network. Such a receiver is exposed to interfering transmissions from all directions, and therefore experiences the maximum possible interference in this symmetric setting. Hence, Equation (63) provides the upper bound of the maximum interference in the network, denoted $I^u_{\max}$.

In this subsection, we show that the expected interference $\mathbf{E}(I)$ over all receiving nodes converges to the same value $I^u_{\max}$ as the network size increases. Consequently, using Equation (45) and Equation (63), a lower bound on the Signal-to-Interference Ratio (SIR) is given by

$$\frac{S}{I_{\max}} = \frac{1}{f(\Delta, \alpha_p)}. \tag{64}$$

A receiver located at the network center experiences interference from all directions, covering a full angular span of 2π radians. Receivers near the boundary, however, may not have active interferers in every direction. For example, a receiver located at a corner of a square-shaped network, such as the one illustrated in Figure 9, experiences interference from approximately one-quarter of the angular domain ($\pi/2$ radians). In this case,

$$I_{\min} = \frac{I_{\max}}{4}. \tag{65}$$

For the vast majority of receivers that lie sufficiently far from network boundaries, the interference they experience is close to that of the central receiver. Let $I(i > \kappa/(1+\Delta))$ denote the interference contributed by all nodes beyond radius κ. This term is linearly related to $\sum_{k=1}^{6} \chi(\Delta, \alpha_p, \kappa, C_k)$, defined in Theorem 5. The ratio of this truncated interference to the total upper-bound interference is bounded by

$$\frac{I(i > \kappa/(1+\Delta))}{I^u_{\max}} \leq \frac{3\sum_{k=1}^{6} \chi(\Delta, \alpha_p, \kappa, C_k)}{\pi\, f(\Delta, \alpha_p)}. \tag{66}$$

When $\kappa \gg 1$, the function $\chi(\Delta, \alpha_p, \kappa, C_k)$ admits the approximation

$$\chi(\Delta, \alpha_p, \kappa, C_k) \simeq \frac{Q(\alpha_p)}{(1+\Delta)^2(\alpha_p - 2)\,\kappa^{\alpha_p - 2}},$$

from which Equation (66) implies

$$\frac{I(i > \kappa/(1+\Delta))}{I^u_{\max}} \propto \kappa^{2-\alpha_p}.$$

Numerical evaluation of this ratio is shown in Figure 12 for various values of κ and realistic path-loss exponents α_p. The ratio decays rapidly toward zero with increasing κ, indicating that receivers located at least κ hops from the network boundary experience interference that is nearly identical to $I_{\max}$. For example, with $\alpha_p = 3$, $n = 10^8$, and $\Delta = 2$, the network contains approximately 3333 links along each axis. Setting $\kappa = 50$, any receiver located at least 50 hops away from every network boundary lies inside a square of side length $3333 - 2 \times 50$. Such a receiver experiences full interference from all directions up to ring κ, whereas nodes closer to the boundary miss at most one quarter of the interferers beyond this radius. Hence, if the residual interference ratio is $I(K > 50) = 0.0345$, as shown in Figure 12, then every receiver obtains at least

$$1 - \frac{3}{4} I(K > 50) = 1 - 0.75 \times 0.0345 = 0.975$$

of the central interference level. Since more than 95% of all receivers lie in this region, the average interference converges to the central value as $n \to \infty$. Nodes at the network boundary experience strictly less interference than $I_{\max}$, with a lower bound of $I_{\min} = I_{\max}/4$. For all other boundary nodes,

$$I_{\min} \leq I \leq I_{\max}.$$

The number of nodes located at least κ hops from all network edges is proportional to $(\sqrt{n} - \kappa)^2$. The remaining boundary nodes number approximately $2\kappa\sqrt{n} + \kappa^2$. Thus, the expected interference satisfies

$$\frac{(\sqrt{n} - \kappa)^2 I_{\max} + (2\kappa\sqrt{n} + \kappa^2) I_{\min}}{n} \leq \mathbf{E}(I) \leq I_{\max}. \tag{67}$$

For fixed κ and $\sqrt{n} \gg \kappa$, the lower bound becomes

$$\lim_{n\to\infty} \frac{(\sqrt{n} - \kappa)^2 I_{\max} + (2\kappa\sqrt{n} + \kappa^2) I_{\min}}{n} = \lim_{n\to\infty} \left(\left(1 - \frac{2\kappa}{\sqrt{n}}\right) I_{\max} + \frac{2\kappa}{\sqrt{n}} I_{\min} \right) = I_{\max}. \tag{68}$$

Therefore,

$$\lim_{n\to\infty} \mathbf{E}(I) = I_{\max}. \tag{69}$$

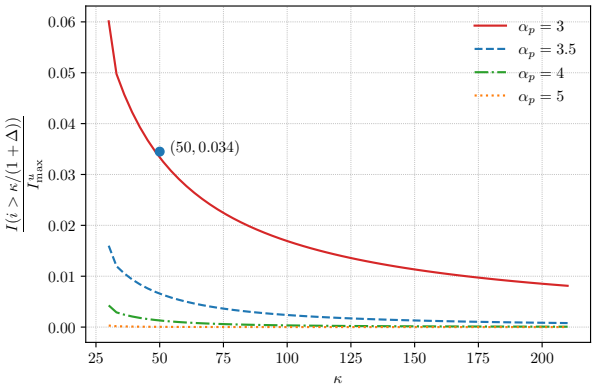

Figure 12: Tail interference ratio $I(i > \kappa/(1+\Delta))/I^u_{\max}$ as a function of κ for several path-loss exponents α_p with $\Delta = 2$. For each α_p, the curve quantifies the fraction of total interference contributed by rings lying beyond the radius $\kappa/(1+\Delta)$ in the hexagonal lattice. Smaller ratios indicate that most interference originates from nearby rings, while larger ratios imply a slower spatial decay.

5.3 Computation and optimization of $\mathbf{E}(C_{\text{eff}})$ over Δ

According to Equation (69), the upper bound of the ratio of the signal to the expected total interference, $S/\mathbf{E}(I)$, can be calculated as $1/f(\Delta, \alpha_p)$, similar to Equation (64):

$$\frac{S}{\mathbf{E}(I)} = \frac{S}{I^u_{\max}} = \frac{1}{f(\Delta, \alpha_p)}\,. \tag{70}$$

Equation (70) shows that $S/\mathbf{E}(I)$ is independent of the transmission distance $r(n)$. For a given path loss exponent α_p and Δ, this ratio is a constant, denoted as K_0. Therefore, the expected link capacity $\mathbf{E}(C_{\text{eff}})$ can be expressed as:

$$\mathbf{E}(C_L) = W\log(1 + \frac{S}{N_0 + \frac{S}{K_0}}) = W\log(1 + \frac{\frac{S}{N_0}}{1 + \frac{S}{N_0 K_0}})\,.$$

For fixed bandwidth W and noise power N_0, increasing the received signal power $S = g_0 P/r(n)^{\alpha_p}$ increases the expected link capacity $\mathbf{E}(C_L)$. Since $S \propto r(n)^{-\alpha_p}$, reducing the transmission range $r(n)$ directly maximizes $\mathbf{E}(C_L)$. Moreover, as shown in [24], minimizing $r(n)$ also maximizes the expected end-to-end point-to-point capacity $\mathbf{E}(C_{\text{P2P}})$. In essence, the optimal strategy is for nodes to communicate with their closest neighbors, even in a multi-hop communication scenario. To optimize C_{P2P}, links with the minimum possible length should be selected to reduce path loss. In this context, we can increase the transmit power such that $\lim_{P\to P_{\max}} N_0/S = 0$ or $\lim_{P\to P_{\max}} N_0/I = 0$. Therefore, the Signal-to-Interference-plus-Noise Ratio (SINR) becomes:

$$\lim_{P\to P_{\max}} \text{SINR} = \frac{S}{I}\,.$$

However, by setting the power level so that $N_0 = I$, we achieve both adequate SINR and energy efficiency:

$$\text{SINR} = \frac{S}{2I}\,.$$

Finally, the lower bound of $\lim_{n\to\infty} \mathbf{E}(C_{\text{eff}})$ is given by:

$$\lim_{n\to\infty} \mathbf{E}(C_L) = W\log(1 + \frac{1}{2f(\Delta, \alpha_p)})\,, \tag{71}$$

Equation (71) conforms to $\Theta(W)$ under the condition that $\alpha_p > 2$. Since $C_{\mathrm{P2P}} = \mathbf{E}(C_{\mathrm{eff}})/\mathbf{E}(h)$, and using Equation (44), we can write:

$$C_{\mathrm{P2P}}(\Delta, \alpha_p) = \frac{W \log(1 + \frac{1}{2f(\Delta, \alpha_p)})}{\mathbf{E}(h)(1+\Delta)^2}. \tag{72}$$

Equation (72) demonstrates that for large-scale ad hoc networks with symmetrically arranged nodes and uniform attenuation patterns, C_{P2P} is asymptotically proportional to $\Theta(W/\mathbf{E}(h))$. We define the normalized P2P capacity C^n_{P2P} as:

$$C^n_{\mathrm{P2P}} = \frac{C_{\mathrm{P2P}}\mathbf{E}(h)}{W} = \frac{\log(1 + \frac{1}{2f(\Delta, \alpha_p)})}{(1+\Delta)^2}. \tag{73}$$

To evaluate the normalized point-to-point capacity C^n_{P2P}, we numerically solved Equation (73) and compared the analytical predictions with simulations based on the full fading model over the symmetric topology of Figure 9 with link length of $r = 31.5$ m. The simulation uses the same hexagonal geometry as the analytical expression: interferer distances are computed using the exact ring–sector functions (ξ, ψ) in Equation (55) and Equation (57), while small-scale fading is modeled by lognormal shadowing ($\sigma = 6$ dB) and Rayleigh fading (unit mean). For each value of Δ, the instantaneous SINR is sampled over 5×10^4 realizations. For typical urban path-loss exponents ($\alpha_p \lesssim 3.5$), the normalized P2P capacity C^n_{P2P} falls in the range 0.15–0.30 bit/s/Hz. This value is obtained under a deliberately simple physical-layer setting (single-antenna, omnidirectional transmission), which keeps the analysis tractable for multi-parameter, large-scale network evaluation. More advanced PHY techniques can increase these values substantially. For example, [35] reports that with 6 transmit antennas and an MMSE MIMO receiver, 0.2–0.3 bit/s/Hz can increase to about 1.5 bit/s/Hz, and [47] shows that beamforming can raise the spectral efficiency further, reaching up to ≈ 3 bit/s/Hz.

The results, shown in Figure 13, demonstrate that C^n_{P2P} is maximized at an optimal reserved–space parameter $\Delta_{\mathrm{opt}} \in (2., 2.5)$, and this maximizer is remarkably stable across different path-loss exponents α_p. This reveals a central insight: *choosing a non-optimal* Δ *can reduce the achievable throughput significantly*, whereas selecting Δ_{opt} ensures that spatial reuse and interference are jointly balanced to maximize capacity. The invariance of Δ_{opt} with respect to α_p further indicates a robust geometric property of the interference field, simplifying network design since the same reserved–space parameter is nearly optimal for a wide range of propagation environments. Substituting Δ_{opt} into Equation (43) yields the optimal spatial reuse factor f_r, representing the number of simultaneously active links per unit area. The resulting values lie between

$$\frac{n}{(3.)^2} \quad \text{and} \quad \frac{n}{2(3.5)^2},$$

meaning roughly $n/10$ to $n/12$ transmitters can operate concurrently on the same frequency band under optimal reuse.

Finally, the curves show that increasing α_p improves C^n_{P2P} in interference-limited ad hoc networks, primarily because stronger distance attenuation reduces long-range interference. The close agreement between analytical and simulated results confirms that the large-scale capacity behavior is governed mainly by geometric interference structure and the path-loss law, whereas precise estimates require incorporating fading.

6 Numerical analysis

To assess the practical relevance of the proposed distributed system architecture, we carry out a numerical evaluation tailored to a realistic large-scale scenario and explicitly quantify end-to-end performance

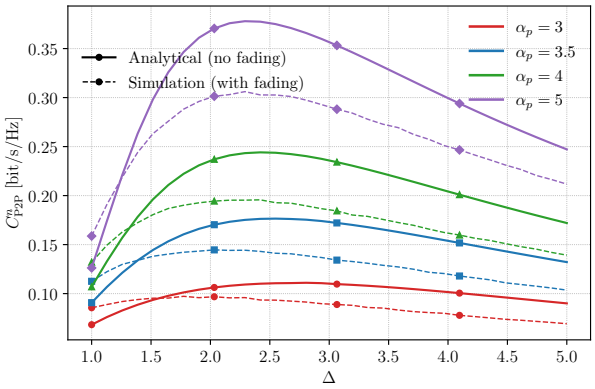

Figure 13: Normalized point-to-point capacity C^n_{P2P} versus the reserved–space parameter Δ for several path-loss exponents α_p. Solid curves with markers show the analytical model (geometry and path loss only), while dashed curves with matching markers show simulations including lognormal shadowing ($\sigma = 6 \quad dB$) and Rayleigh fading (unit mean).

in terms of throughput, delay, spectrum usage, and energy feasibility. We consider a hypothetical megacity with a population of 100 million inhabitants. While such cities do not yet exist, projections indicate that rapid urbanization could lead to megacities of this scale by the end of the 21st century [46]. This extreme scenario highlights the potential of fully distributed networking to handle very high node densities and vast network diameters.

For concreteness, we assume a population density of 4,800 persons/km^2, similar to that of Montréal, Canada [15], and an average building height of 15 m (approximately four floors) [21]. Normalizing per floor yields an effective density of 1,200 persons/km^2 per floor. We assume that each person may act as a wireless node, with a distance-dependent interaction probability as described in Section 4.

6.1 Hop count and spatial scale

We first compute the area per person A_p from the normalized population density:

$$A_p \times 1{,}200 = 1 \text{ km}^2 \implies A_p = \frac{1 \text{ km}^2}{1{,}200} = \frac{25^2 \times 2^2}{3} \text{ m}^2.$$

Assuming each user occupies a regular hexagon in a hexagonal lattice, the area A_p satisfies

$$A_p = \frac{3\sqrt{3}}{2} l_0^2,$$

where l_0 is the hexagon side length. In this lattice, the distance between adjacent nodes, d_0, is related to l_0 via $d_0 = \sqrt{3}\, l_0$. Substituting $l_0 = d_0/\sqrt{3}$ yields

$$A_p = \frac{3\sqrt{3}}{2} \left(\frac{d_0}{\sqrt{3}} \right)^2 = \frac{\sqrt{3}}{2} d_0^2.$$

Equating this with the computed A_p gives

$$\frac{\sqrt{3}}{2} d_0^2 = \frac{25^2 \times 2^2}{3} \implies d_0 = \sqrt{961.94} \approx 31 \text{ m}.$$

Following the empirical measurements in [3], we take the reference distance $\beta_0 = 313$ m, yielding the normalized parameter

$$\beta = \frac{\beta_0}{d_0} = \frac{313}{31} \approx 10.1.$$

In [3], the social-interaction probability over distance follows a power law with exponent $\alpha = 3.05$. Substituting (α, β, n) into the closed-form upper bound in Section 4.1.3 on the expected hop count, we obtain

$$\mathbf{E}(h) < 86.$$

The corresponding expected communication range is

$$\mathbf{E}(h)\, d_0 < 2.7 \text{ km}.$$

The network diameter D (maximum source–destination separation) is estimated as

$$D = d_0 \sqrt{2\Big(\frac{\sqrt{3}(n/4)}{2}\Big)} = d_0\, \frac{\sqrt{n}\, 3^{0.25}}{2} \approx 204 \text{ km}.$$

Although the network diameter is on the order of hundreds of kilometers, the *typical* end-to-end communication path spans only about 1.3% of this distance. This striking disparity highlights the critical role of realistic, distance-dependent interaction probabilities: while the network is physically large, most communications remain highly local. As emphasized in this work and in [24], ignoring this behavioral locality has historically led to overly pessimistic assessments of multi-hop ad hoc networks and a systematic underestimation of their true scalability potential.

6.2 Throughput, rate services, and delay performance

For an urban environment with high building density, we adopt a path-loss exponent $\alpha_p = 4$. Using the interference analysis in Section 5.3 and the optimized reserved-space parameter Δ_{opt}, the maximal normalized P2P capacity is

$$C^n_{\text{P2P}} \approx 0.20 \text{ bit/s/Hz}$$

(see Figure 13). For a total system bandwidth of $W = 200$ MHz allocated to the distributed network, the average end-to-end P2P rate, , by using Equation (73) is

$$C_{\text{P2P}} = \frac{C^n_{\text{P2P}} W}{\mathbf{E}(h)} \approx 0.47 \text{ Mbps}.$$

Even with this modest average rate per P2P connection, each user can obtain several gigabytes of data per day:

$$C_{\text{daily}} = 86{,}400 \times C_{\text{P2P}} \approx 4 \text{ GBytes/day}.$$

If all frequency resources are temporarily allocated to a single active link, the peak link capacity is

$$C_L^{\max} = C^n_{\text{P2P}}\, W\, (1 + \Delta_{\text{opt}})^2 \approx 400 \text{ Mbps},$$

where $(1 + \Delta_{\text{opt}})^2 \approx (3.2)^2$ corresponds to $\Delta_{\text{opt}} \approx 2.2$ (see Equation (73)). When the spectrum is divided among simultaneously active links, the average per-link capacity is

$$C_L^{\text{av}} = C^n_{\text{P2P}}\, W \approx 40 \text{ Mbps}.$$

Consider a high-bandwidth video service with packet size $L_{\text{pkt}} = 576$ bytes and a frame rate of 30 fps. We focus on the *transmission component* of the end-to-end delay over a typical P2P connection spanning $\mathbf{E}(h)$ hops. Assuming that, at each hop, the active link can temporarily access the full available bandwidth, the minimum achievable average end-to-end transmission delay is given by

$$\tau^{\text{av}}_{\min} = \frac{8 L_{\text{pkt}}\, \mathbf{E}(h)}{C_L^{\max}} \approx 1ms.$$

which is far below the 33 ms frame interval. This expression represents a lower bound, as practical operation incurs additional queuing and medium-access delays at each relay. Propagation delay is negligible in this short range link cases. With average link capacity C_L^{av}, the mean delay is

$$\tau_{\text{av}}^{\text{av}} = \frac{8L_{\text{pkt}}\,\mathbf{E}(h)}{C_L^{\text{av}}}, \approx 10ms$$

This delay remains well below typical real-time service thresholds. Even for worst-case long-distance communications—which occur with very low probability, as shown in Section 4.1.3, since the vast majority of connections are local—the resulting end-to-end delay remains bounded, with the maximum delay given by

$$\tau_{\text{max}}^{\text{max}} = \frac{8L_{\text{pkt}}\,D}{d_0\,C_L^{\text{max}}}, = 115ms$$

which remains acceptable for most non-interactive services. This level of performance for most communication (expected value) is comparable to that reported for 5G networks, whose end-to-end delays typically fall in the range of 30–35 ms [39].

6.3 Energy efficiency and spectral efficiency

We now examine the energy consumption per node. Under the optimal operating point, each node is active for approximately $24/(3.2)^2 \approx 2.4$ hours per day, since each active link occupies a fraction $1/(1+\Delta_{\text{opt}})^2$ of the total time due to spatial resource sharing. We consider a carrier frequency $f_c = 2$ GHz, a path-loss exponent $\alpha_p = 4$, and the optimal reserved-space parameter Δ_{opt}. For this configuration, the normalized point-to-point capacity is $C_{\text{P2P}}^n = 0.2$. Using Equation (73), where $f(\Delta_{\text{opt}}, \alpha_p) = N/S$, the resulting target signal-to-noise ratio is $S/N = 6$. Accordingly, the link budget yields the following path-loss term:

$$L_{\text{path}} = 10\alpha_p \log_{10}(d_0) + 20\log_{10}(f_c) + 32.45 \approx 98.1 \text{ dB}.$$

The corresponding noise power is

$$N_0 = kTW = 1.38 \times 10^{-23} \times 300 \times 200 \times 10^6 \approx 8.28 \times 10^{-13} \text{ W},$$

and the required received signal power is

$$S = \frac{S}{N}\, N_0 \approx 5 \times 10^{-12} \text{ W}.$$

Compensating for path loss, the required transmit power is

$$P_t = S \times 10^{L_{\text{path}}/10} \approx 5 \times 10^{-12} \times 10^{9.81} \approx 32.3 \text{ mW}.$$

If a node actively transmits for approximately 2.4 hours per day, the daily energy consumption per node is

$$E_{\text{day}} = P_t \times 2.4 \text{ h} \approx 77.5 \text{ mWh}.$$

Assuming a typical smartphone battery voltage of 3.7 V, this corresponds to

$$E_{\text{day}} \approx 21 \text{ mAh},$$

which is negligible compared to a typical smartphone battery capacity of 4,000 mAh. This allows operation for many days without recharging, an important advantage in emergency situations or infrastructure outages.

Given a daily traffic volume of approximately 4 GBytes per user, the resulting energy cost for end-to-end delivery of one bit is on the order of

$$\mathcal{E}_{\text{bit}} \approx 8.8 \text{ nJ/bit},$$

which is dramatically lower than the best reported values for 5G downlink ($\approx$ 20 nJ/bit) and LTE ($\approx$ 70 nJ/bit) [53]. This highlights the intrinsic energy advantage of short-range, interference-managed multi-hop communication.

The spectral efficiency achieved mainly through dense resource reuse with population density 4,800 persons/km^2 is

$$F = \frac{C^n_{\mathrm{P2P}} \times \rho}{\mathbf{E}(h)} = \frac{0.2 \times 4{,}800}{86} \approx 11.1 \text{ bit/s/Hz/km}^2.$$

As the population density ρ increases, the normalized point-to-point capacity C^n_{P2P} remains fixed, while the expected hop count $\mathbf{E}(h)$ scales at most with the typical link length, i.e., $\mathbf{E}(h) = \mathcal{O}(\sqrt{\rho})$ when interaction patterns do not become more localized. In this conservative case, the spectral efficiency scales as $\rho/\sqrt{\rho} = \sqrt{\rho}$. In practice, however, increasing density typically leads to more localized communications, causing the expected hop count to grow slowly or remain nearly constant. Consequently, the spectral efficiency can scale almost linearly with population density ρ, reflecting the strong potential for aggressive spatial resource reuse. This demonstrates that the achieved spectral efficiency remains robust—and can even improve—as the network becomes denser.

6.4 Discussion: Practical implications and potential

These results show that a very large-scale distributed network, operating with limited spectrum and a simple physical layer (no MIMO and no beamforming), can deliver user data volumes comparable to many current cellular offerings. It is important to emphasize that this value represents an idealized upper bound. In practice, several factors must be taken into account. Link utilization cannot be continuously full, and increased contention may lead to higher waiting times and packet losses. Consequently, even under favorable conditions, only a fraction of this capacity—on the order of 50%–70%—is likely to be achievable in a stable network. Moreover, suboptimal scheduling, heterogeneous traffic demand (with some areas experiencing significantly higher load than average), and the need for protocol overhead and guard intervals between transmitters further reduce the effective throughput. Deviations from the assumed symmetric topology also make optimal resource sharing more complex and harder to achieve in practice. These effects are unavoidable and must be acknowledged.

At the same time, the reported values do not capture the full potential of large-scale distributed networking. As discussed in Section 5.3 and demonstrated in [35, 47], advanced transmission techniques such as beamforming and MIMO can increase C^n_{P2P} from 0.2–0.3 bit/s/Hz to 2–3 bit/s/Hz, far exceeding what is achievable with an omnidirectional physical layer. In fact, the main point behind achieving these numerical results is not the optimality or simplicity of the considered scenario. Even higher performance could be achieved under realistic conditions if the network is properly designed. The observed performance gains stem from two fundamental properties that hold for virtually any network topology and physical-layer technology.

First, we show that realistic interaction patterns yield expected hop counts and communication distances that are nearly two orders of magnitude smaller than classical pessimistic estimates, translating directly into substantial improvements in P2P capacity and power efficiency. This property is largely independent of the specific network topology: for networks with the same physical dimensions and node density, the expected number of hops remains approximately the same regardless of node position. As a result, the widely cited performance degradation attributed to multi-hop communication is largely a consequence of overly pessimistic modeling assumptions.

Second, the fact that shorter links optimize overall network performance [19, 24] creates significant potential for aggressive spatial reuse and ultra-low-power operation, effectively alleviating traditional battery-life concerns and, in many cases, outperforming cellular architectures. This property is independent of the particular network or physical-layer technology. To illustrate this effect, in our model the typical link length is approximately 30 m. Although cellular link lengths in LTE or 5G depend on

cell type, even an optimistic average link length of 300 m leads to a dramatic difference in path loss. For example, with a path-loss exponent $\alpha_p = 4$, the ratio is

$$\left(\frac{300}{30}\right)^4 = 10^4.$$

Even though part of this loss is mitigated by antenna height and directional gain in cellular systems, with an expected hop count of $\mathbf{E}(h) < 100$ in massive-scale distributed networks, the total power consumption can still be significantly lower. A similar argument applies to spatial reuse: since the reuse factor scales approximately with the square of the link length, the reuse efficiency in the distributed network is about two orders of magnitude higher than in the cellular case. This gain is sufficient to offset the resource reduction caused by multi-hop forwarding and enables performance competitive with cellular systems in terms of aggregate throughput. Furthermore, this short-link regime naturally identifies millimeter-wave technologies— whose performance is strongest at short ranges—as ideal candidates for distributed networks, especially given the orders-of-magnitude larger bandwidths they offer compared to conventional sub-6 GHz systems.

Therefore, the key insights of this work directly address classical concerns regarding the practicality of large-scale ad hoc networking. Consequently, the use of a symmetric topology and a simplified physical-layer model should not be interpreted as an oversimplification. Rather, it is a deliberate choice to expose the fundamental large-scale behavior, design principles, and performance potential of distributed networking—insights that cannot be captured through narrow or small-scale analyses.

7 Conclusion and future work

In this work, we derived closed-form performance bounds for very large-scale distributed ad hoc networks, providing explicit numerical estimates of the expected hop count, link-level and end-to-end capacity, delay, energy consumption, and spectral efficiency. The analysis combines stochastic geometry, Riemann sum approximation, integration, and convex optimization to obtain tractable closed-form upper bounds on the expected hop count, aggregate interference, and achievable transmission capacity under optimal resource sharing.

A key finding is that, under realistic interaction patterns, the expected hop count and communication distance are nearly two orders of magnitude smaller than classical pessimistic estimates, leading directly to substantial gains in throughput and energy efficiency. Moreover, the analysis shows that the in optimal operating regime in distributed networking corresponds to forwarding data, the energy required for a single long-range cellular transmission can exceed—by several orders of magnitude—the aggregate energy of many short multi-hop transmissions. As a result, even with on the order of 10^2 forwarding hops per connection, the total power consumption of a distributed P2P session remains well below that of state-of-the-art centralized systems such as LTE and 5G. The same short-link principle applies to spatial reuse. Since reuse efficiency scales approximately with the square of the link length, distributed networks achieve reuse gains of nearly two orders of magnitude compared to cellular architectures. These properties are inherent to distributed wireless networking and are largely independent of the specific network topology or physical-layer technology. Consequently, large-scale distributed networks can sustain per-user data volumes comparable to current cellular systems while operating with limited spectrum and extremely low transmit power. These insights directly address long-standing concerns regarding the practicality of large-scale ad hoc networking. Accordingly, the use of a symmetric topology is a deliberate analytical choice, designed to isolate and expose the fundamental large-scale behavior, core design principles, and intrinsic performance limits of distributed wireless networks.

Overall, this work demonstrates that large-scale distributed ad hoc networks are not only theoretically scalable but also practically competitive with infrastructure-based systems, particularly in dense urban environments. Future research will extend this framework to random node placements and will

incorporate advanced routing and interference coordination mechanisms to further refine performance bounds and guide the design of deployable large-scale systems.

Appendix A Geometric characterization of interfering nodes and interference bounds

Theorem 1 (Distance between central element and elements in a sector)**.** Given that x_j is the angle between the perpendicular bisector of the sector and the line segment connecting the central node to node j (as shown in Figure A.1), where $\frac{-\pi}{6} < x_j \leq \frac{\pi}{6}$, and r is the distance between immediate neighbors, the distance between the central element to any element j is given by:

$$d_j^i = \frac{(1+\Delta) i r \cos(\frac{\pi}{6})}{\cos(x_j)}\,. \tag{A.1}$$

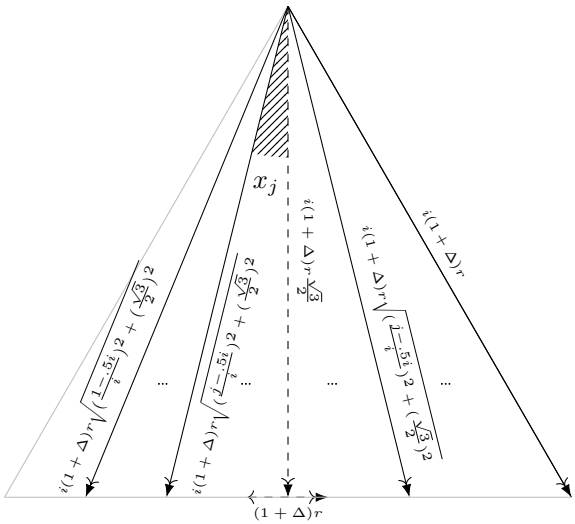

Figure A.1: Distance computation for interferers in the i-th ring of a hexagonal lattice, shown over a single $\frac{\pi}{6}$ sector by symmetry. The ring index i determines the nominal radial distance $i(1+\Delta)r$, while the index j enumerates nodes within the ring at different angular offsets on both sides of the symmetry axis. Nodes with $j < i/2$ and $j > i/2$ appear symmetrically and yield identical interference contributions. Distances are obtained by combining the vertical component $i(1+\Delta)r\frac{\sqrt{3}}{2}$ with a horizontal offset proportional to $\mid j - \frac{i}{2} \mid (1+\Delta)r$, where $1 \leq j \leq i$.

Proof. The distance between the central element and element j, in a sector from ring i^{th}, defined as d_j^i, as depicted in Figure A.1, given by

$$d_j^i = i(1+\Delta)r\sqrt{(\frac{j-0.5i}{i})^2 + (\frac{\sqrt{3}}{2})^2}, \quad 1 \leq j \leq i\,. \tag{A.2}$$

Considering x_j as the angle shown in Figure A.1, we have

$$\cos(x_j) = \frac{i(1+\Delta)r\frac{\sqrt{3}}{2}}{i(1+\Delta)r\sqrt{(\frac{j-0.5i}{i})^2 + (\frac{\sqrt{3}}{2})^2}} = \frac{\sqrt{3}}{2\sqrt{(\frac{j-0.5i}{i})^2 + (\frac{\sqrt{3}}{2})^2}}. \tag{A.3}$$

By substituting $\cos(x_j)$ from Equation (A.3) into Equation (A.2), we obtain:

$$d_j^i = \frac{(1+\Delta) i r \cos(\frac{\pi}{6})}{\cos(x_j)}. \tag{A.4}$$

□

Theorem 2 (Distance between Interfering Transmitters and the Central Receiver)**.** For a node j in the first sector, where $0 < \varphi \leq \frac{\pi}{3}$, and the i^{th} sector, the distance is calculated as:

$$r_j^i = r\sqrt{(\frac{i(1+\Delta)\cos(\frac{\pi}{6})}{\cos(\varphi - \frac{\pi}{6})} - \cos(\varphi_j))^2 + \sin^2(\varphi)}\,. \tag{A.5}$$

Proof. From Theorem 1, if x_j is the angle between the perpendicular bisector of the sector and the segment connecting the central node to node j, where $\frac{-\pi}{6} < x_j \leq \frac{\pi}{6}$, the distance d_j^i is given by:

$$d_j^i = \frac{(1+\Delta)ir\cos(\frac{\pi}{6})}{\cos(x_j)}. \tag{A.6}$$

For $i > 1$, as depicted in Figure A.2, we have:

$$\frac{r_j^i}{2} = \sqrt{(\frac{d_j^i}{2} - \frac{r}{2}\cos(\varphi_j))^2 + (\frac{r}{2}\sin(\varphi))^2}.$$

According to Figure A.2, the relationship between x_j and φ_j for $0 \leq \varphi_j \leq \frac{\pi}{3}$ is $x_j = \varphi_j - \frac{\pi}{6}$. Substituting d_j^i from Equation (A.6), the distance r_j^i of any interfering transmitter node from the center receiver, for $0 < \varphi_j \leq \frac{\pi}{3}$, is

$$r_j^i = r\sqrt{(\frac{i(1+\Delta)\cos(\frac{\pi}{6})}{\cos(\varphi - \frac{\pi}{6})} - \cos(\varphi_j))^2 + \sin^2(\varphi)}\,. \tag{A.7}$$

□

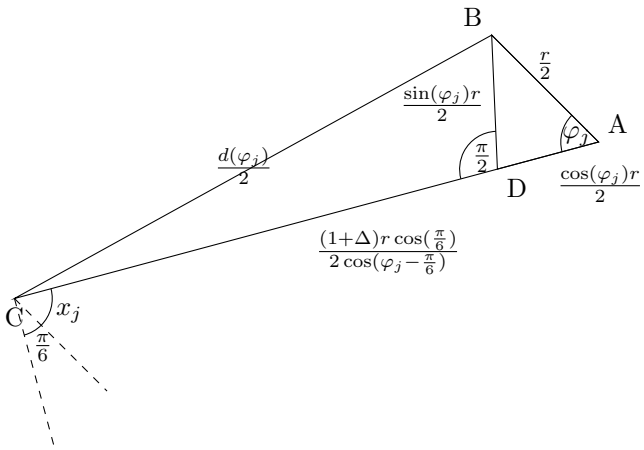

Figure A.2: Geometric construction for computing distances to node j-th on the i-th ring within a hexagonal lattice sector. The angular index x_j (angle φ_j) parameterizes node positions, and the resulting distance $d(\varphi_j)$ is obtained from projections along the sector geometry.

Theorem 3 (Distance to Interfering Transmitters)**.** Consider a symmetric network arranged in a hexagonal lattice, as depicted in Figure 11. For rings with $i \geq 2$, each ring is divided into six identical sectors, each containing i interfering transmitters. The distance from the central receiver to an interfering transmitter in ring i, sector k, at angle φ_j is given by:

$$r_{ijk} = r\,\psi(i, \varphi_j, k), \tag{A.8}$$

where

$$\psi(i, \varphi_j, k) = \left[(\frac{i(1+\Delta)\cos(\frac{\pi}{6})}{\cos(\varphi_j - \frac{\pi}{6})} - \cos(\varphi_j + \frac{(k-1)\pi}{3}))^2 + \sin^2(\varphi_j + \frac{(k-1)\pi}{3})\right]^{\frac{1}{2}}. \tag{A.9}$$

Proof.

In sector $k = 1$, the angle φ_j is determined by:

$$\cos(\varphi_j) = \frac{i-j}{2i\sqrt{(\frac{j-0.5i}{i})^2 + (\frac{\sqrt{3}}{2})^2}}, \quad j = 1, 2, \ldots, i. \tag{A.10}$$

For other sectors $k > 1$ with $\frac{(k-1)\pi}{3} \leq \varphi \leq \frac{k\pi}{3}$, the expressions are obtained by applying a phase shift of $\frac{(k-1)\pi}{3}$ to $\cos(\varphi_j)$ and $\sin(\varphi_j)$ in Equation (A.5) of Theorem 2, and by factoring out $\psi(i, \varphi_j, k)$ as Equation (A.9), Equation (A.8) is achieved. □

Theorem 4 ($\psi(i, \varphi, k)$ approximation)**.** For any sectors of $1 \leq k \leq 6$ and $\varphi \in [0, \frac{\pi}{3}]$ the lower bound of the $\psi(i, \varphi, k)$ could be written as

$$\psi(i, \varphi, k) \geq (i(1+\Delta) - C_k)\frac{\cos(\frac{\pi}{6})}{\cos(\varphi - \frac{\pi}{6})}, \tag{A.11}$$

where $C_k \in \{\frac{1}{\sqrt{3}} + \frac{1}{2}, \frac{1}{2}, \frac{-1}{2}, \frac{-1}{2}, \frac{1}{2}, \frac{1}{\sqrt{3}} + \frac{1}{2}\}$.

Proof. We start with the expression:

$$\frac{\cos(\varphi - \frac{\pi}{6})\cos(\varphi + \frac{(k-1)\pi}{3})}{\cos(\frac{\pi}{6})} = \frac{\cos(2\varphi - \frac{\pi}{6} + \frac{(k-1)\pi}{3}) + \cos(\frac{\pi}{6} + \frac{(k-1)\pi}{3})}{2\cos(\frac{\pi}{6})}.$$

As shown in Table A.1, the maximum of the expression for any sector is presented as C_k. Thus, we can write:

$$i(1+\Delta)\frac{\cos(\frac{\pi}{6})}{\cos(\varphi - \frac{\pi}{6})} - \cos(\varphi + \frac{(k-1)\pi}{3}) \geq$$
$$i(1+\Delta)\frac{\cos(\frac{\pi}{6})}{\cos(\varphi - \frac{\pi}{6})} - C_k\frac{\cos(\frac{\pi}{6})}{\cos(\varphi - \frac{\pi}{6})}.$$

Table A.1: Function extreme values per sector.

K	Equation per sector	Max value (C_k)	Min value
1	$\frac{\cos(2\varphi - \frac{\pi}{6}) + \cos(\frac{\pi}{6})}{2\cos(\frac{\pi}{6})}$	$\frac{1}{\sqrt{3}} + \frac{1}{2}$	$\frac{1}{2}$
2	$\frac{\cos(2\varphi + \frac{\pi}{6}) + \cos(\frac{\pi}{2})}{2\cos(\frac{\pi}{6})}$	$\frac{1}{2}$	$-\frac{1}{2}$
3	$\frac{\cos(2\varphi + \frac{\pi}{2}) + \cos(\frac{5\pi}{6})}{2\cos(\frac{\pi}{6})}$	$-\frac{1}{2}$	$-(\frac{1}{\sqrt{3}} + \frac{1}{2})$
4	$\frac{\cos(2\varphi + \frac{5\pi}{6}) + \cos(\frac{7\pi}{6})}{2\cos(\frac{\pi}{6})}$	$-\frac{1}{2}$	$-(\frac{1}{\sqrt{3}} + \frac{1}{2})$
5	$\frac{\cos(2\varphi + \frac{7\pi}{6}) + \cos(\frac{3\pi}{2})}{2\cos(\frac{\pi}{6})}$	$\frac{1}{2}$	$-\frac{1}{2}$
6	$\frac{\cos(2\varphi + \frac{3\pi}{2}) + \cos(\frac{11\pi}{6})}{2\cos(\frac{\pi}{6})}$	$\frac{1}{\sqrt{3}} + \frac{1}{2}$	$\frac{1}{2}$

Squaring both sides of the inequality, adding $\sin^2(\varphi)$, and then taking the square root, we obtain Equation (A.12):

$$\psi(i, \varphi, k) = (i(1+\Delta)\frac{\cos(\frac{\pi}{6})}{\cos(\varphi - \frac{\pi}{6})} - \cos(\varphi + \frac{(k-1)\pi}{3}))^2 + \sin^2(\varphi + \frac{(k-1)\pi}{3}) \geq$$
$$((i(1+\Delta) - C_k)^2\frac{\cos^2(\frac{\pi}{6})}{\cos^2(\varphi - \frac{\pi}{6})} + \sin^2(\varphi + \frac{(k-1)\pi}{3}))^{\frac{1}{2}}$$
$$\geq (i(1+\Delta) - C_k)\frac{\cos(\frac{\pi}{6})}{\cos(\varphi - \frac{\pi}{6})}. \tag{A.12}$$

□

Theorem 5 (Upper Bound of Interference from Distant Rings)**.** For a symmetric network arranged in a hexagonal lattice, the total interference from all rings beyond a threshold $i > \frac{\kappa}{1+\Delta}$, where $\kappa \gg 1$, has an upper bound given by:

$$I(i > \frac{\kappa}{1+\Delta}) < \frac{3Pg_0Q(\alpha_p)}{\pi r^{\alpha_p}} \sum_{k=1}^{6} \chi(\Delta, \alpha_p, \kappa, C_k), \tag{A.13}$$

with:

$$\chi(\Delta, \alpha_p, \kappa, C_k) = \frac{Q(\alpha_p)(1+\Delta)^{-1}(\alpha_p - 1)(\left\lceil \frac{\kappa}{1+\Delta} \right\rceil - 0.5) - C_k(1+\Delta)^{-2}}{\left[(1+\Delta)(\left\lceil \frac{\kappa}{1+\Delta} \right\rceil - 0.5) - C_k\right]^{\alpha_p - 1} (\alpha_p - 2)(\alpha_p - 1)}. \tag{A.14}$$

where:

- C_k are constants specific to each sector k provided in Table A.1,
- $Q(\alpha_p) = \int_0^{\frac{\pi}{3}} \frac{\cos^{\alpha_p}(\varphi - \frac{\pi}{6})}{\cos^{\alpha_p}(\frac{\pi}{6})} \, d\varphi$.

Proof. For $i \gg 1$, the sum over j and k in the interference $I(i)$ can be approximated using the Riemann integral. The discrete sum:

$$\frac{\pi}{3i} \sum_{k=1}^{6} \sum_{j=1}^{i} \frac{i}{\psi(i, \varphi_j, k)^{\alpha_p}} \approx \sum_{k=1}^{6} \int_0^{\frac{\pi}{3}} \frac{i}{\psi(i, \varphi, k)^{\alpha_p}} \, d\varphi, \tag{A.15}$$

where $\psi(i, \varphi, k)$ is as defined in Equation (57).

According to geometric considerations (details in Equation (A.11)), for the k^{th} sector, $\psi(i, \varphi, k)$ has a lower bound:

$$\psi(i, \varphi, k) \geq \frac{i(1+\Delta) - C_k}{\cos(\frac{\pi}{6})} \cos(\varphi - \frac{\pi}{6}). \tag{A.16}$$

Substituting the lower bound into the integral, we obtain:

$$\begin{aligned} I(i) &< \frac{3Pg_0}{\pi r^{\alpha_p}} \sum_{k=1}^{6} \int_0^{\frac{\pi}{3}} \frac{i}{\left[\frac{i(1+\Delta) - C_k}{\cos(\frac{\pi}{6})} \cos(\varphi - \frac{\pi}{6})\right]^{\alpha_p}} \, d\varphi \\ &= \frac{3Pg_0}{\pi r^{\alpha_p}} \sum_{k=1}^{6} \frac{i}{[i(1+\Delta) - C_k]^{\alpha_p}} \int_0^{\frac{\pi}{3}} \frac{\cos^{\alpha_p}(\varphi - \frac{\pi}{6})}{\cos^{\alpha_p}(\frac{\pi}{6})} \, d\varphi \\ &= \frac{3Pg_0Q(\alpha_p)}{\pi r^{\alpha_p}} \sum_{k=1}^{6} \frac{i}{[i(1+\Delta) - C_k]^{\alpha_p}}, \end{aligned} \tag{A.17}$$

where $Q(\alpha_p)$ is defined as:

$$Q(\alpha_p) = \int_0^{\frac{\pi}{3}} \frac{\cos^{\alpha_p}(\varphi - \frac{\pi}{6})}{\cos^{\alpha_p}(\frac{\pi}{6})} \, d\varphi. \tag{A.18}$$

To compute the upper bound of the total interference from rings beyond $i > \frac{\kappa}{1+\Delta}$, we consider the sum:

$$I(i > \frac{\kappa}{1+\Delta}) < \frac{3Pg_0Q(\alpha_p)}{\pi r^{\alpha_p}} \sum_{i=\left\lceil \frac{\kappa}{1+\Delta} \right\rceil}^{\infty} \sum_{k=1}^{6} \frac{i}{[i(1+\Delta) - C_k]^{\alpha_p}}. \tag{A.19}$$

We define $l(r)$ as:

$$l(r) = \sum_{k=1}^{6} \frac{r}{[r(1+\Delta) - C_k]^{\alpha_p}}. \tag{A.20}$$

Since $l(r)$ is a convex decreasing function for $r \geq \left\lceil \frac{\kappa}{1+\Delta} \right\rceil$ and $\kappa \gg C_k$, we can use the integral test for convergence:

$$\sum_{i=\left\lceil \frac{\kappa}{1+\Delta} \right\rceil}^{\infty} l(i) \leq \int_{\left\lceil \frac{\kappa}{1+\Delta} \right\rceil - 0.5}^{\infty} l(r)\, dr. \tag{A.21}$$

Integrating $l(r)$, we get:

$$\int l(r)\, dr = C_0 - \sum_{k=1}^{6} \frac{(1+\Delta)(\alpha_p - 1)r - C_k}{(1+\Delta)^2 \left[r(1+\Delta) - C_k\right]^{\alpha_p - 1} (\alpha_p - 2)(\alpha_p - 1)}, \tag{A.22}$$

where C is the constant of integration.

Therefore, the upper bound of $I(i > \frac{\kappa}{1+\Delta})$ is:

$$I(i > \frac{\kappa}{1+\Delta}) < \frac{3Pg_0}{\pi r^{\alpha_p}} \sum_{k=1}^{6} \chi(\Delta, \alpha_p, \kappa, C_k), \tag{A.23}$$

where $\chi(\Delta, \alpha_p, \kappa, C_k)$ is as defined in Equation (A.14).

This completes the proof. □

Appendix B Series to integral approximation

Theorem 6 (Mean Value Location for Convex Decreasing Functions)**.** Let $f : [a, b] \to \mathbb{R}$ be a continuous, convex, and strictly decreasing function on the closed interval $[a, b]$. Let M be the mean value of f over $[a, b]$, i.e.,

$$M = \frac{1}{b-a} \int_a^b f(x)\, dx.$$

Then, if c is a point in (a, b) such that $f(c) = M$, c is located in the left half of the interval $[a, b]$, i.e., $c \leq \frac{a+b}{2}$.

Proof. Let $f : [a, b] \to \mathbb{R}$ be a continuous, convex, and strictly decreasing function, and let M be the mean value of f over $[a, b]$:

$$M = \frac{1}{b-a} \int_a^b f(x)\, dx.$$

Suppose $c \in (a, b)$ satisfies $f(c) = M$. We aim to show $c \leq \frac{a+b}{2}$. Assume, for contradiction, that $c > \frac{a+b}{2}$. Since f is strictly decreasing, $f(x) > M$ for $x < c$ and $f(x) < M$ for $x > c$. Given f is convex, Jensen's inequality implies:

$$f(\frac{a+b}{2}) \leq \frac{1}{b-a} \int_a^b f(x)\, dx = M.$$

However, if $c > \frac{a+b}{2}$, the integral would be weighted more towards lower function values, contradicting $f(c) = M$. Thus, c must satisfy $c \leq \frac{a+b}{2}$. □

Theorem 7 (Infinite integral for Convex Decreasing Functions)**.** Let $f : [a, b] \to \mathbb{R}$ be a continuous, convex, and strictly decreasing function on the closed interval $[a, b]$. Let M be the mean value of f over $[a, b]$, i.e.,

$$M = \frac{1}{b-a} \int_a^b f(x)\, dx.$$

Then, if c is a point in (a, b) such that $f(c) = M$, c is located in the left half of the interval $[a, b]$, i.e., $c \leq \frac{a+b}{2}$. For a convex decreasing function $f(x)$, $\sum_{i=a}^{\infty} f(i) \leq \int_{a-\frac{1}{2}}^{\infty} f(x)\, dx$

Proof. Based on Theorem 7, for any interval $[i - \frac{1}{2}, i + \frac{1}{2}]$, $f(i) \leq \int_{i-\frac{1}{2}}^{i+\frac{1}{2}} f(x)\, dx$. Therefore

$$\sum_{i=a}^{\infty} f(i) \leq \sum_{i=a}^{\infty} \int_{i-\frac{1}{2}}^{i+\frac{1}{2}} f(x)\, dx \leq \int_{a-\frac{1}{2}}^{\infty} f(x)\, dx$$

. □

Theorem 8 (P_0 series to integral)**.** For $\alpha > 2$,

$$\sum_{i=1}^{\sqrt{\frac{n}{\pi}}} \frac{i}{(i+\beta)^{\alpha}} \geq \int_1^{\sqrt{\frac{n}{\pi}}} \frac{r}{(r+\beta)^{\alpha}}\, dr - \frac{(\alpha-1)^{\alpha-1}}{\alpha^{\alpha}\beta^{\alpha-1}}\,.$$

Proof. Considering $f(r) = \frac{r}{(r+\beta)^{\alpha}}$, $\frac{d}{dr} f(r)$ is given by

$$\frac{d}{dr} f(r) = \frac{\beta + (1-\alpha)r}{(r+\beta)^{\alpha+1}}\,.$$

$f(r)$ has only one maximum at $r = \frac{\beta}{\alpha-1}$. For any $i \leq \left\lfloor \frac{\beta}{\alpha-1} \right\rfloor$:

$$\sum_{i=1}^{\lfloor \frac{\beta}{\alpha-1} \rfloor} f(i) = \sum_{i=1}^{\lfloor \frac{\beta}{\alpha-1} \rfloor} \frac{i}{(i+\beta)^{\alpha}} \geq \int_0^{\lfloor \frac{\beta}{\alpha-1} \rfloor} \frac{r}{(r+\beta)^{\alpha}}\, dr\,,$$

and for $i \geq \left\lfloor \frac{\beta}{\alpha-1} \right\rfloor$:

$$\sum_{i=\lfloor \frac{\beta}{\alpha-1} \rfloor+1}^{\sqrt{\frac{n}{\pi}}} f(i) = \sum_{i=\lfloor \frac{\beta}{\alpha-1} \rfloor+1}^{\sqrt{\frac{n}{\pi}}} \frac{i}{(i+\beta)^{\alpha}} \geq \int_{\lfloor \frac{\beta}{\alpha-1} \rfloor}^{\sqrt{\frac{n}{\pi}}} \frac{r}{(r+\beta)^{\alpha}}\, dr\,.$$

By summing up both cases, we have

$$\sum_{i=1}^{\sqrt{\frac{n}{\pi}}} \frac{i}{(i+\beta)^{\alpha}} \geq \int_0^{\sqrt{\frac{n}{\pi}}} \frac{r}{(r+\beta)^{\alpha}}\, dr - \int_{\lfloor \frac{\beta}{\alpha-1} \rfloor}^{\lfloor \frac{\beta}{\alpha-1} \rfloor+1} \frac{r}{(r+\beta)^{\alpha}}\, dr\,.$$

Furthermore, $\int f(r)\, dr$ computed as

$$\int \frac{r}{(r+\beta)^{\alpha}}\, dr = -\frac{(r+\beta)^{1-\alpha}((\alpha-1)r+\beta)}{(\alpha-1)(\alpha-2)} + C\,, \tag{B.24}$$

that by using Equation (B.24), we have

$$\int_{\lfloor \frac{\beta}{\alpha-1} \rfloor}^{\lfloor \frac{\beta}{\alpha-1} \rfloor+1} \frac{r}{(r+\beta)^{\alpha}}\, dr \leq \frac{(\alpha-1)^{\alpha-1}}{\alpha^{\alpha}\beta^{\alpha-1}}\,.$$

Consequently,

$$\sum_{i=1}^{\sqrt{\frac{n}{\pi}}} \frac{i}{(i+\beta)^\alpha} \geq \left(\int_0^{\sqrt{\frac{n}{\pi}}} \frac{r}{(r+\beta)^\alpha}\, dr - \frac{(\alpha-1)^{\alpha-1}}{\alpha^\alpha \beta^{\alpha-1}}\right). \tag{B.25}$$

□

Theorem 9 (Approximate $\mathbf{E}(h)$ series with an integral)**.** For $\alpha > 2$,

$$\sum_{i=2}^{\sqrt{\frac{n}{\pi}}} \int_0^{\frac{\pi}{6}} \frac{i^2}{\left(\frac{i\cos(\frac{\pi}{6})}{\cos(\varphi)} + \beta\right)^\alpha} d\varphi \leq \int_2^{\sqrt{\frac{n}{\pi}}} \int_0^{\frac{\pi}{6}} \frac{r^2}{\left(\frac{r\cos(\frac{\pi}{6})}{\cos(\varphi)} + \beta\right)^\alpha} d\varphi\, dr + \frac{(\alpha-2)^\alpha (2\sqrt{3} + \frac{4\pi}{3})}{3\beta^{\alpha-2}\alpha^\alpha}. \tag{B.26}$$

Proof.

Considering the function $f(r,\varphi) = \frac{r^2}{\left(\frac{r\cos(\frac{\pi}{6})}{\cos(\varphi)} + \beta\right)^\alpha}$,

$$\frac{\mathrm{d}f(r,\varphi)}{\mathrm{d}r} = \frac{r\left((2-\alpha)\frac{r\cos(\frac{\pi}{6})}{\cos(\varphi)} + 2\beta\right)}{\left(\frac{r\cos(\frac{\pi}{6})}{\cos(\varphi)} + \beta\right)^{\alpha+1}}$$

The maximum of $f(r,\varphi)$ occurs at $r_{\max} = \frac{2\beta\cos(\varphi)}{(\alpha-2)\cos(\frac{\pi}{6})}$. $f(r,\varphi)$ is increasing for $r \leq \frac{2\beta\cos(\varphi)}{(\alpha-2)\cos(\frac{\pi}{6})}$ and decreasing for higher values of r. We can thus write:

$$\sum_{i=2}^{\lfloor \frac{2\beta\cos(\varphi)}{(\alpha-2)\cos(\frac{\pi}{6})} \rfloor} \int_0^{\frac{\pi}{6}} \frac{i^2}{\left(\frac{i\cos(\frac{\pi}{6})}{\cos(\varphi)} + \beta\right)^\alpha} d\varphi \leq \int_2^{\lfloor \frac{2\beta\cos(\varphi)}{(\alpha-2)\cos(\frac{\pi}{6})} \rfloor + 1} \int_0^{\frac{\pi}{6}} \frac{r^2}{\left(\frac{r\cos(\frac{\pi}{6})}{\cos(\varphi)} + \beta\right)^\alpha} d\varphi\, dr\,, \tag{B.27}$$

and for $r \geq \frac{2\beta\cos(\varphi)}{(\alpha-2)\cos(\frac{\pi}{6})}$, we have:

$$\sum_{\lfloor \frac{2\beta\cos(\varphi)}{(\alpha-2)\cos(\frac{\pi}{6})} \rfloor + 1}^{\sqrt{\frac{n}{\pi}}} \int_0^{\frac{\pi}{6}} \frac{i^2}{\left(\frac{i\cos(\frac{\pi}{6})}{\cos(\varphi)} + \beta\right)^\alpha} d\varphi \leq \int_{\lfloor \frac{2\beta\cos(\varphi)}{(\alpha-2)\cos(\frac{\pi}{6})} \rfloor}^{\sqrt{\frac{n}{\pi}}} \int_0^{\frac{\pi}{6}} \frac{r^2}{\left(\frac{r\cos(\frac{\pi}{6})}{\cos(\varphi)} + \beta\right)^\alpha} d\varphi\, dr. \tag{B.28}$$

Summing up Equations (B.27) and (B.28), we get:

$$\begin{aligned}\sum_{i=2}^{\sqrt{\frac{n}{\pi}}} \int_0^{\frac{\pi}{6}} \frac{i^2}{\left(\frac{i\cos(\frac{\pi}{6})}{\cos(\varphi)} + \beta\right)^\alpha} d\varphi \leq \Bigg(&\int_2^{\sqrt{\frac{n}{\pi}}} \int_0^{\frac{\pi}{6}} \frac{r^2}{\left(\frac{r\cos(\frac{\pi}{6})}{\cos(\varphi)} + \beta\right)^\alpha} d\varphi\, dr \\ &+ \int_{\lfloor \frac{2\beta\cos(\varphi)}{(\alpha-2)\cos(\frac{\pi}{6})} \rfloor}^{\lfloor \frac{2\beta\cos(\varphi)}{(\alpha-2)\cos(\frac{\pi}{6})} \rfloor + 1} \int_0^{\frac{\pi}{6}} \frac{r^2}{\left(\frac{r\cos(\frac{\pi}{6})}{\cos(\varphi)} + \beta\right)^\alpha} d\varphi\, dr\Bigg).\end{aligned} \tag{B.29}$$

We then have:

$$\begin{aligned}&\int_{\lfloor \frac{2\beta\cos(\varphi)}{(\alpha-2)\cos(\frac{\pi}{6})} \rfloor}^{\lfloor \frac{2\beta\cos(\varphi)}{(\alpha-2)\cos(\frac{\pi}{6})} \rfloor + 1} \int_0^{\frac{\pi}{6}} \frac{r^2}{\left(\frac{r\cos(\frac{\pi}{6})}{\cos(\varphi)} + \beta\right)^\alpha} d\varphi\, dr \\ &\qquad \leq \int_0^{\frac{\pi}{6}} \frac{4\beta^2\cos^2(\varphi)/\cos^2(\frac{\pi}{6})}{\left(\frac{2\beta}{\alpha-2} + \beta\right)^\alpha} d\varphi = \frac{(\alpha-2)^\alpha (2\sqrt{3} + \frac{4\pi}{3})}{3\beta^{\alpha-2}\alpha^\alpha}.\end{aligned} \tag{B.30}$$

It means the upper bound of the $\mathbf{E}(h)$ series could be given the below integral as

$$\sum_{i=2}^{\sqrt{\frac{n}{\pi}}} \int_0^{\frac{\pi}{6}} \frac{i^2}{\left(\frac{i\cos(\frac{\pi}{6})}{\cos(\varphi)} + \beta\right)^\alpha} d\varphi \leq \int_2^{\sqrt{\frac{n}{\pi}}} \int_0^{\frac{\pi}{6}} \frac{r^2}{\left(\frac{r\cos(\frac{\pi}{6})}{\cos(\varphi)} + \beta\right)^\alpha} d\varphi\, dr + \frac{(\alpha-2)^\alpha (2\sqrt{3} + \frac{4\pi}{3})}{3\beta^{\alpha-2}\alpha^\alpha}. \tag{B.31}$$

□

Appendix C Extreme values and upper bounds related to $\mathbf{E}(h)$

Theorem 10. By moving away from the corner of the network to the center on the line of $x = y$ as Figure C.3 so that the minimum distance of the source node from all corners considered as $\kappa\beta$, then $\frac{P_0^{min}}{P_0^{\kappa\beta}}$ is given by

$$\frac{P_0^{min}}{P_0^{\kappa\beta}} \geq \begin{cases} 1 - \frac{1+\frac{1}{\pi}}{\kappa+1}, & \text{if } \alpha \geq 3 \\ 1 - \frac{0.75\alpha - 1.25 + \frac{1}{\pi}}{(\kappa+1)^{\alpha-2}}, & \text{if } \alpha \approx 3, \alpha < 3\,. \end{cases} \tag{C.32}$$

Proof.

The integral for P_0 can be rewritten as:

$$\begin{aligned} \int_1^{\sqrt{\frac{n}{\pi}}} \frac{r}{(r+\beta)^\alpha}\, dr &= \int_1^{\kappa\beta} \frac{r}{(r+\beta)^\alpha}\, dr + \int_{\kappa\beta}^{\sqrt{\frac{n}{\pi}}} \frac{r}{(r+\beta)^\alpha}\, dr \\ &= \frac{1}{(\alpha-1)(\alpha-2)} \left(\frac{\alpha - 1 + \beta}{(1+\beta)^{\alpha-1}} - \frac{(\alpha-1)\sqrt{\frac{n}{\pi}} + \beta}{(\sqrt{\frac{n}{\pi}} + \beta)^{\alpha-1}} \right) \end{aligned}$$

If we consider the $P_0^{\kappa\beta}$ as the P_0 constant for the point on the line $x = y$ that is at least $\kappa\beta$ away from all network corners, and call A as the effective area for the integral, we should have $P_0(\oint_A P(a)\, da + C(\alpha,\beta)) = 1$. Here, $P(a)$ is the interaction probability, and $C(\alpha,\beta)$ is the offset value of converting series to integral. On the other hand, for the P_0^{min} the area of integral is the $\int_0^{\sqrt{\frac{n}{\pi}}} \frac{r}{(r+\beta)^\alpha}\, dr \approx \int_0^{\infty} \frac{r}{(r+\beta)^\alpha}\, dr$. Therefore, we can write,

$$\frac{P_0^{min}}{P_0^{\kappa\beta}} = \frac{\oint_A P(a)\, da + C(\alpha,\beta)}{\int_0^{\infty} \frac{r}{(r+\beta)^\alpha}\, dr + C(\alpha,\beta)}$$

As depicted in Figure C.3, the integral for the effective area of A could be written so that

$$\begin{aligned} \frac{P_0^{min}}{P_0^{\kappa\beta}} &= \frac{\frac{1}{\beta^{\alpha-2}} - \frac{(\alpha-2)(\alpha-1)^\alpha}{\alpha^\alpha \beta^{\alpha-1}} - \frac{3((\alpha-1)\kappa\beta+\beta)}{4((\kappa+1)\beta)^{\alpha-1}} + \frac{1}{\pi}\int_{\kappa\beta}^{\infty} \frac{\arcsin(\frac{\kappa\beta}{r})r}{\pi(r+\beta)^\alpha}\, dr}{\frac{1}{\beta^{\alpha-2}} - \frac{(\alpha-2)(\alpha-1)^\alpha}{\alpha^\alpha \beta^{\alpha-1}}} \\ &\approx 1 - \frac{3((\alpha-1)\kappa+1)}{4(\kappa+1)^{\alpha-1}} + \frac{\beta^{\alpha-2}}{\pi} \int_{\kappa\beta}^{\infty} \frac{\arcsin(\frac{\kappa\beta}{r})r}{\pi(r+\beta)^\alpha}\, dr\,. \end{aligned}$$

since always $\frac{P_0^{min}}{P_0^{\kappa\beta}} \leq 1$, always:

$$\frac{3((\alpha-1)\kappa+1)}{4(\kappa+1)^{\alpha-1}} \geq \frac{\beta^{\alpha-2}}{\pi} \int_{\kappa\beta}^{\infty} \frac{\arcsin(\frac{\kappa\beta}{r})r}{\pi(r+\beta)^\alpha}\, dr\,.$$

Therefore, we can write:

$$\frac{P_0^{min}}{P_0^{\kappa\beta}} = 1 - (1-C)\frac{3((\alpha-1)\kappa+1)}{4(\kappa+1)^{\alpha-1}}$$

where $0 \leq C \leq 1$. Now, we consider $f(\alpha) = \frac{3((\alpha-1)\kappa+1)}{4(\kappa+1)^{\alpha-1}}$, if we show $\frac{df}{d\alpha} \leq 0$ for all $\alpha \geq 3$, then by increasing α, $\frac{P_0^{min}}{P_0^{\kappa\beta}}$ increases. We have

$$\frac{df}{d\alpha} = \frac{3((1-(\alpha-1)^2)\kappa^2 + 2\kappa - \alpha + 1)}{4(\kappa+1)^\alpha}\,,$$

that shows that for any $\kappa \geq 1$ and $\alpha \geq 3$, $\frac{P_0^{min}}{P_0^{\kappa\beta}}$ is increasing with respect to α. Therefore, $\left.\frac{P_0^{min}}{P_0^{\kappa\beta}}\right|_{\alpha=3}$ is a lower bound for all $\alpha \geq 3$. Furthermore,

$$\frac{1}{\pi}\int_{\kappa\beta}^{\infty}\frac{\arcsin(\frac{\kappa\beta}{r})r}{\pi(r+\beta)^3}\,dr = \frac{\kappa^2}{\pi\beta}\left((\frac{-\frac{\kappa\arcsin(\frac{\kappa x}{|x+\kappa|}+\frac{1}{|x+\kappa|})}{\sqrt{\kappa^2-1}-\kappa^2\sqrt{\kappa^2-1}}-\frac{\sqrt{1-\kappa^2}}{-\kappa^2x+x-\kappa^3+\kappa}}{2}-\frac{\arcsin(x)}{2(x+\kappa)^2})\right|_{x=0}^{x=1}\right).$$

Could be shown the result of the integral if $\kappa \gg 1$, is approximated by

$$\frac{\beta}{\pi}\int_{\kappa\beta}^{\infty}\frac{\arcsin(\frac{\kappa\beta}{r})r}{(r+\beta)^3}\,dr = \frac{(0.5-\frac{1}{\pi})\kappa-\frac{1}{\pi}}{(\kappa+1)\kappa},$$

that if $\alpha \geq 3$;

$$\begin{aligned}\frac{P_0^{min}}{P_0^{\kappa\beta}} &\geq \frac{3((\alpha-1)\kappa+1)}{4(\kappa+1)^{\alpha-1}}+\frac{(0.5-\frac{1}{\pi})\kappa-\frac{1}{\pi}}{(\kappa+1)\kappa}\\ &\geq 1-\frac{3(2\kappa+1)}{4(\kappa+1)^2}+\frac{(0.5-\frac{1}{\pi})\kappa-\frac{1}{\pi}}{(\kappa+1)^2} \geq 1-\frac{(1+\frac{1}{\pi})\kappa+\frac{1}{\pi}+.75}{(\kappa+1)^2}.\end{aligned}$$

Finally, the simplified ratio is given by

$$\frac{P_0^{min}}{P_0^{\kappa\beta}} \geq 1-\frac{(1+\frac{1}{\pi})}{\kappa+1}. \tag{C.33}$$

For $\alpha \leq 3$, also could be written that

$$\begin{aligned}\frac{P_0^{min}}{P_0^{\kappa\beta}} &\geq 1-\frac{3((\alpha-1)\kappa+1)}{4(\kappa+1)^{\alpha-1}}+\frac{\beta^{\alpha-3}(0.5-\frac{1}{\pi})\kappa-\frac{1}{\pi}}{(\kappa+1)\kappa} \geq\\ &1-\frac{3((\alpha-1)\kappa+1)}{4(\kappa+1)^{\alpha-1}}+\frac{\beta^{\alpha-3}(0.5-\frac{1}{\pi})\kappa-\frac{1}{\pi}}{(\kappa+1)^2} \geq\\ &\frac{P_0^{min}}{P_0} \geq 1-\frac{3((\alpha-1)\kappa+1)+((\kappa+1)\beta)^{\alpha-3}((0.5-\frac{1}{\pi})\kappa-\frac{1}{\pi})}{4(\kappa+1)^{\alpha-1}}.\end{aligned}$$

If $\alpha \approx 3$, $((\kappa+1)\beta)^{\alpha-3} \approx 1$, then

$$\frac{P_0^{min}}{P_0^{\kappa\beta}} \geq 1-\frac{.75\alpha-1.25+\frac{1}{\pi}}{(\kappa+1)^{\alpha-2}}. \tag{C.34}$$

Hence, for both cases we have

$$\frac{P_0^{min}}{P_0^{\kappa\beta}} \geq \begin{cases}1-\frac{1+\frac{1}{\pi}}{\kappa+1}, & \text{if } \alpha \geq 3\\ 1-\frac{0.75\alpha-1.25+\frac{1}{\pi}}{(\kappa+1)^{\alpha-2}}, & \text{if } \alpha \approx 3, \alpha < 3.\end{cases} \tag{C.35}$$

□

Theorem 11. Let $f : \mathbb{R}^2 \to \mathbb{R}$ be a positive, radially decreasing function, i.e., $f(r,\vartheta) > 0$ and $\frac{\partial f}{\partial r} < 0$ for all sufficiently large r. Consider the integral of f over a square S centered at the origin with side length L, as depicted in Figure C.4.

Then, the integral satisfies the following bounds:

$$\sum_{k=1}^{12}\int_{\theta_k}^{\theta_k+\frac{\pi}{6}}\int_0^{R_k} f(r,\vartheta)\,r\,dr\,d\vartheta \leq \int_S f(r,\vartheta)\,dA \leq \int_C f(r,\vartheta)\,dA,$$

where:

- C is a circle centered at the origin with radius $R = \frac{L}{\sqrt{\pi}}$,
- The lower bound is obtained by dividing S into 12 sectors, each spanning an angle of $\frac{\pi}{6}$. Specifically, 8 sectors have radius $R_k = \frac{L}{2}$ and 4 sectors have radius $R_k = \frac{L}{\sqrt{3}}$.

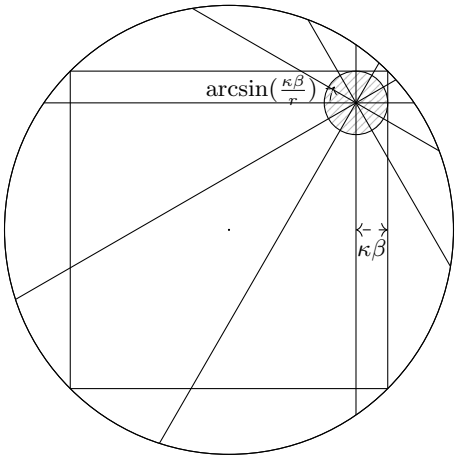

Figure C.3: Geometric configuration used to bound edge effects in Theorem 10. The square represents the finite network region, and the circumscribed circle defines the maximum possible distance to the boundary. The source node is placed along the diagonal $x = y$, at a minimum distance $\kappa\beta$ from all network corners.

Proof. Consider the square S centered at the origin with side length L. We partition S into 12 sectors, each with an angular span of $\frac{\pi}{6}$ radians.

Lower bound:

- Among these 12 sectors, 8 sectors can be inscribed within the square with a radius $R = \frac{L}{2}$.
- The remaining 4 sectors are inscribed with a radius $R = \frac{L}{\sqrt{3}}$.

Since $f(r, \vartheta)$ is positive and radially decreasing, the integral of f over each sector is maximized when the radius R_k is as large as possible within the sector. Therefore, the sum of the integrals over these 12 sectors provides a lower bound for the integral over the entire square:

$$\int_S f(r, \vartheta)\, dA \geq \sum_{k=1}^{12} \int_{\theta_k}^{\theta_k + \frac{\pi}{6}} \int_0^{R_k} f(r, \vartheta)\, r\, dr\, d\vartheta.$$

We ensure that the combined area of these sectors is entirely contained within the square. Since f is positive and decreases with r, the integral over these sectors provides a conservative (lower) estimate of the integral over the entire square.

Upper bound:

- Approximate the square S with a circle C centered at the origin such that both have the same area. The radius of this circle is $R = \frac{L}{\sqrt{\pi}}$, since $\text{Area}(C) = \pi R^2 = L^2$.
- For any point inside the square but outside the circle C, the radial distance r satisfies $r > \frac{L}{\sqrt{\pi}}$. Given that $f(r, \vartheta)$ is decreasing with r, the value of f at these points is less than or equal to f at corresponding points inside C.

The integral of f over the square is bounded above by the integral of f over the circle since any area outside the circle but inside the square contributes less to the integral than the corresponding area inside the circle. Hence, integrating over the circle gives an upper bound for the integral over the square.

$$\int_S f(r, \vartheta)\, dA \leq \int_C f(r, \vartheta)\, dA.$$

Combining both bounds, we obtain:

$$\sum_{k=1}^{12} \int_{\theta_k}^{\theta_k+\frac{\pi}{6}} \int_0^{R_k} f(r,\vartheta)\, r\, dr\, d\vartheta \le \int_S f(r,\vartheta)\, dA \le \int_C f(r,\vartheta)\, dA.$$

□

Theorem 12. [Geometric relations of r_k] If we consider a point inside a circle of radius R, and divide the circle into 6 pair of sectors each of sectors covering $\frac{\pi}{6}$ concerning that point, then for any arbitrary point inside the circle

$$\sum_{k=1}^{6} r_{1k}^2 + r_{2k}^2 = 12R^2$$

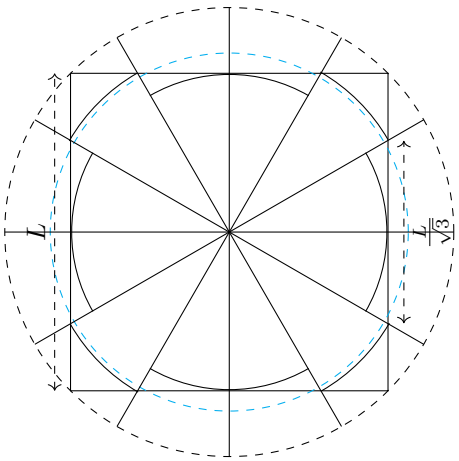

Figure C.4: Geometric construction used to derive upper and lower bounds on the integral of a radially decreasing function over a square (Theorem 11). The square of side length L represents the network region. For the lower bound, the square is partitioned into 12 angular sectors of width $\pi/6$: eight sectors admit a maximal inscribed radius $R_k = L/2$, while the remaining four sectors admit $R_k = L/\sqrt{3}$. For the upper bound, the square is enclosed by an equal-area circle of radius $R = L/\sqrt{\pi}$.

Proof. Consider a point inside a circle with radius R, and divide the circle into 12 sectors (6 pairs), each covering $\frac{\pi}{6}$. We aim to show that the sum of the squares of the distances from the node to the boundaries of these sectors is $12R^2$.

First, consider the distances r_{1k} and r_{2k} in a pair of sectors. as shown in Figure 6. For r_{1k}andr_{2k}, we have:

$$(r_{1k} + a\cos(\varphi_k + \theta))^2 + a\sin(\varphi + \theta) = R^2\,, \text{and}$$

$$(r_{2k} - a\cos(\varphi + \theta))^2 + a\sin(\varphi + \theta) = R^2$$

By summing these equations, we obtain,

$$r_{1k}^2 + r_{2k}^2 + 2a^2 + 2(r_{1k} - r_{2k})\cos(\varphi_k + \theta) = 2R^2\,.$$

Due to symmetry, we have:

$$r_{2k} - a\cos(\varphi + \theta) = r_{1k} + a\cos(\varphi + \theta)\,,$$

which implies

$$r_{2k} - r_{1k} = 2a\cos(\varphi + \theta)\,.$$

Substituting this back into our sum, we get

$$r_{1k}^2 + r_{2k}^2 = 2R^2 + 2a^2 \cos(2(\varphi_k + \theta)) \,.$$

Since we have 6 pairs of such sectors, the total sum is

$$\sum_{k=1}^{6} r_{1k}^2 + r_{2k}^2 = \sum_{k=1}^{6} 2R^2 + 2a^2 \cos(2(\varphi_k + \theta)) \,.$$

As $\varphi_k \in \{0, \cdots, \frac{(k-1)\pi}{6}, \cdots, \frac{5\pi}{6}\}$, the sum of the cosines over a complete cycle averages out to zero, regardless of the values of a and θ, leaving us with:

$$\sum_{k=1}^{6} r_{1k}^2 + r_{2k}^2 = 12R^2 \,. \qquad \square$$

References

[1] Giusi Alfano, Michele Garetto, Emilio Leonardi, and Valentina Martina. Capacity scaling of wireless networks with inhomogeneous node density: Lower bounds. IEEE/ACM Transactions on Networking, 18(5):1624–1636, 2010.

[2] Bita Azimdoost, Hamid R Sadjadpour, and JJ Garcia-Luna-Aceves. Capacity of wireless networks with social behavior. IEEE Transactions on Wireless Communications, 12(1):60–69, 2012.

[3] Lars Backstrom, Eric Sun, and Cameron Marlow. Find me if you can: improving geographical prediction with social and spatial proximity. In Proceedings of the 19th international conference on World wide web, pages 61–70, 2010.

[4] Michael Bailey, Rachel Cao, Theresa Kuchler, Johannes Stroebel, and Arlene Wong. Social connectedness: Measurement, determinants, and effects. Journal of Economic Perspectives, 32(3):259–280, 2018.

[5] Michael Bailey, Patrick Farrell, Theresa Kuchler, and Johannes Stroebel. Social connectedness in urban areas. Journal of Urban Economics, 118:103264, 2020.

[6] C Balasubramanian and R Lal Raja Singh. Iot based energy management in smart grid under price based demand response based on hybrid fho-rernn approach. Applied Energy, 361:122851, 2024.

[7] Simon Elias Bibri, Alahi Alexandre, Ayyoob Sharifi, and John Krogstie. Environmentally sustainable smart cities and their converging ai, iot, and big data technologies and solutions: an integrated approach to an extensive literature review. Energy Informatics, 6(1):9, 2023.

[8] Leonardo Bonati, Salvatore D'Oro, Michele Polese, Stefano Basagni, and Tommaso Melodia. Intelligence and learning in o-ran for data-driven nextg cellular networks. IEEE Communications Magazine, 59(10):21–27, 2021.

[9] Matthias R. Brust and Bogdan M. Strimbu. A networked swarm model for uav deployment in the assessment of forest environments. arXiv preprint arXiv:1607.04439, 2016.

[10] Y. Cao, Y. Zhang, Y. Wang, et al. Computational intelligence in multi-uav cooperative networks: Recent advances and future directions. IEEE Transactions on Cognitive Communications and Networking, 2024.

[11] Elin Chen, Junfu Chen, Ali Wagdy Mohamed, Bi Wang, Zhendong Wang, and Yang Chen. Swarm intelligence application to uav aided iot data acquisition deployment optimization. IEEE Access, 8:175660–175668, 2020.

[12] Mingzhe Chen, Deniz Gündüz, Kaibin Huang, Walid Saad, Mehdi Bennis, Aneta Vulgarakis Feljan, and H. Vincent Poor. Distributed learning in wireless networks: Recent progress and future challenges. IEEE Journal on Selected Areas in Communications, 39(12):3579–3605, 2021.

[13] Zirui Chen, Zhaoyang Zhang, and Zhaohui Yang. Big ai models for 6g wireless networks: Opportunities, challenges, and research directions. IEEE Wireless Communications, pages 1–9, 2024.

[14] Zairan Cheng and Ying Liu. Performance study and optimization of 3d-manet:: A new analytical perspective based on zipf's law. Wireless Communications and Mobile Computing, 2022, 2022.

[15] Ville de Montréal. Statistics montreal. https://montreal.ca/en/topics/statistics-montreal. Accessed: [Insert date].

[16] Massimo Franceschetti, Olivier Dousse, NC David, and Patrick Thiran. Closing the gap in the capacity of wireless networks via percolation theory. IEEE Transactions on Information Theory, 53(3):1009–1018, 2007.

[17] Massimo Franceschetti, Marco Donald Migliore, and Paolo Minero. The capacity of wireless networks: Information-theoretic and physical limits. IEEE Transactions on Information Theory, 55(8):3413–3424, 2009.

[18] Luoyi Fu, Wentao Huang, Xiaoying Gan, Feng Yang, and Xinbing Wang. Capacity of wireless networks with social characteristics. IEEE Transactions on Wireless Communications, 15(2):1505–1516, 2015.

[19] Piyush Gupta and Panganmala R Kumar. The capacity of wireless networks. IEEE Transactions on information theory, 46(2):388–404, 2000.

[20] Mohammad Hassan, Ji-Hoon Park, and Min-Ho Han. Enhancing livestock management with iot-based wireless sensor networks: a comprehensive approach for health monitoring, location tracking, behavior analysis, and environmental optimization. Journal of Sustainable Urban Futures, 13(6):34–46, 2023.

[21] Jaroslav Holis and Pavel Pechac. Elevation dependent shadowing model for mobile communications via high altitude platforms in built-up areas. IEEE Transactions on Antennas and Propagation, 56(4):1078–1084, 2008.

[22] Xumin Huang, Peichun Li, Hongyang Du, Jiawen Kang, Dusit Niyato, Dong In Kim, and Yuan Wu. Federated learning-empowered ai-generated content in wireless networks. IEEE Network, pages 1–1, 2024.

[23] Mohsen Karimzadeh Kiskani, Bita Azimdoost, and Hamid R. Sadjadpour. Effect of social groups on the capacity of wireless networks. IEEE Transactions on Wireless Communications, 15(1):3–13, 2016.

[24] R Khalvandi and B Sanso. The feasibility of ultra large-scale distributed networks in symmetrical network typologies. Les Cahiers du GERAD ISSN, 711:2440, 2024.

[25] Gautier Krings, Francesco Calabrese, Carlo Ratti, and Vincent D Blondel. Urban gravity: a model for inter-city telecommunication flows. Journal of Statistical Mechanics: Theory and Experiment, 2009(07):L07003, 2009.

[26] Heorhii Kuchuk and Eduard Malokhvii. Integration of iot with cloud, fog, and edge computing: A review. Advanced Information Systems, 8(2):65–78, 2024.

[27] Renaud Lambiotte, Vincent D Blondel, Cristobald De Kerchove, Etienne Huens, Christophe Prieur, Zbigniew Smoreda, and Paul Van Dooren. Geographical dispersal of mobile communication networks. Physica A: Statistical Mechanics and its Applications, 387(21):5317–5325, 2008.

[28] Bibb Latané, James H Liu, Andrzej Nowak, Michael Bonevento, and Long Zheng. Distance matters: Physical space and social impact. Personality and Social Psychology Bulletin, 21(8):795–805, 1995.

[29] Si-Hyeon Lee and Sae-Young Chung. Capacity scaling of wireless ad hoc networks: Shannon meets maxwell. IEEE Transactions on Information Theory, 58(3):1702–1715, 2012.

[30] Moshe Levy and Jacob Goldenberg. The gravitational law of social interaction. Physica A: Statistical Mechanics and its Applications, 393:418–426, 2014.

[31] Jinyang Li, Charles Blake, Douglas SJ De Couto, Hu Imm Lee, and Robert Morris. Capacity of ad hoc wireless networks. In Proceedings of the 7th annual international conference on Mobile computing and networking, pages 61–69, 2001.

[32] David Liben-Nowell, Jasmine Novak, Ravi Kumar, Prabhakar Raghavan, and Andrew Tomkins. Geographic routing in social networks. Proceedings of the National Academy of Sciences, 102(33):11623–11628, 2005.

[33] Jia Liu, Jianjian Xiang, Yongjun Jin, Renhua Liu, Jining Yan, and Lizhe Wang. Boost precision agriculture with unmanned aerial vehicle remote sensing and edge intelligence: A survey. Remote Sensing, 13(21):4387, 2021.

[34] Lei Liu, Min Sheng, Junyu Liu, Yuzhou Li, and Jiandong Li. Performance analysis of scma ad hoc networks: A stochastic geometry approach. In 2016 IEEE Wireless Communications and Networking Conference, pages 1–6, 2016.

[35] Jing Ma, Ying Jun Zhang, Xin Su, and Yan Yao. On capacity of wireless ad hoc networks with mimo mmse receivers. IEEE Transactions on Wireless Communications, 7(12):5493–5503, 2008.

[36] Maurilio Matracia, Mustafa A Kishk, and Mohamed-Slim Alouini. Aerial base stations for global connectivity: Is it a feasible and reliable solution? IEEE Vehicular Technology Magazine, 2023.

[37] Wided Moulahi, Imen Jdey, Tarek Moulahi, Moatsum Alawida, and Abdulatif Alabdulatif. A blockchain-based federated learning mechanism for privacy preservation of healthcare iot data. Computers in Biology and Medicine, 167:107630, 2023.

[38] Yuqiang Ning and Lili Du. Robust and resilient equilibrium routing mechanism for traffic congestion mitigation built upon correlated equilibrium and distributed optimization. Transportation research part B: methodological, 168:170–205, 2023.

[39] AA OLUWALEKE. Performance metrics evaluation and technical comparative analysis of 5g and fibre optics networks technology for real-time video streaming. Journal of Engineering Research and Development, 2025.

[40] Jukka-Pekka Onnela, Samuel Arbesman, Marta C González, Albert-László Barabási, and Nicholas A Christakis. Geographic constraints on social network groups. PLoS one, 6(4):e16939, 2011.

[41] Ayfer Ozgur, Olivier Lévêque, and NC David. Hierarchical cooperation achieves optimal capacity scaling in ad hoc networks. IEEE Transactions on information theory, 53(10):3549–3572, 2007.

[42] Hamid R Sadjadpour, Zheng Wang, et al. The capacity of wireless ad hoc networks with multi-packet reception. IEEE Transactions on Communications, 58(2):600–610, 2010.

[43] Sujie Shao, Juntao Zheng, Shaoyong Guo, Feng Qi, and I Xuesong Qiu. Decentralized ai-enabled trusted wireless network: A new collaborative computing paradigm for internet of things. IEEE Network, 37(2):54–61, 2023.

[44] Yandong Shi, Lixiang Lian, Yuanming Shi, Zixin Wang, Yong Zhou, Liqun Fu, Lin Bai, Jun Zhang, and Wei Zhang. Machine learning for large-scale optimization in 6g wireless networks. IEEE Communications Surveys and Tutorials, 25(4):2088–2132, 2023.

[45] Stefan Thurner and Benedikt Fuchs. Physical forces between humans and how humans attract and repel each other based on their social interactions in an online world. PLoS one, 10(7):e0133185, 2015.

[46] Department of Economic United Nations and Social Affairs. World urbanization prospects: The 2018 revision. https://population.un.org/wup/, 2018. Accessed: [Insert date].

[47] Rahul Vaze and Robert W Heath. Transmission capacity of ad-hoc networks with multiple antennas using transmit stream adaptation and interference cancellation. IEEE Transactions on Information theory, 58(2):780–792, 2012.

[48] Yuhua Wang, Laixian Peng, Renhui Xu, and Shuai Cheng. The upper bound of capacity for multi-mode networking with multi-beam antenna array. In 2021 7th International Conference on Computer and Communications (ICCC), pages 2143–2148. IEEE, 2021.

[49] Steven P Weber, Xiangying Yang, Jeffrey G Andrews, and Gustavo De Veciana. Transmission capacity of wireless ad hoc networks with outage constraints. IEEE transactions on information theory, 51(12):4091–4102, 2005.

[50] Zhiqing Wei, Huici Wu, Xin Yuan, Sai Huang, and Zhiyong Feng. Achievable capacity scaling laws of three-dimensional wireless social networks. IEEE Transactions on Vehicular Technology, 67(3):2671–2685, 2018.

[51] Shiyang Wu, Andrew CM Austin, Ameer Ivoghlian, Akshat Bisht, and Kevin I-Kai Wang. Long range wide area network for agricultural wireless underground sensor networks. Journal of Ambient Intelligence and Humanized Computing, 14(5):4903–4919, 2023.

[52] Wen Wu, Mushu Li, Kaige Qu, Conghao Zhou, Xuemin Shen, Weihua Zhuang, Xu Li, and Weisen Shi. Split learning over wireless networks: Parallel design and resource management. IEEE Journal on Selected Areas in Communications, 41(4):1051–1066, 2023.

[53] Dongzhu Xu, Ao Li, Xiaojiang Guo, Jiacheng Liu, Yuefeng Zhang, Xinyu Xie, Yu Wu, Xuanzhe Zhang, Kai Liu, Zhi-Li Liu, and Yunxin Liu. Understanding operational 5g: A first measurement study on its coverage, performance and energy consumption. In Proceedings of the ACM SIGCOMM 2020 Conference, page 479–494, 2020.

[54] Dachao Yu, Yao Sun, Yuetai Li, Lei Zhang, and Muhammad Ali Imran. Communication resource allocation of raft in wireless network. IEEE Sensors Journal, 23(17):19398–19408, 2023.

[55] Yang Zhou, Yan Shi, and Shanzhi Chen. Capacity and delay analysis for large social-aware mobile ad hoc wireless networks. Applied Sciences, 10(5):1719, 2020.

[56] Alphan Şahin. Distributed learning over a wireless network with non-coherent majority vote computation. IEEE Transactions on Wireless Communications, 22(11):8020–8034, 2023.